Received: 10 September 2020 | Revised: 7 December 2020 | Accepted: 16 December 2020

DOI: 10.1002/nano.202000142

REVIEW

Nano Select WILEY

Recent advances in the Van der Waals epitaxy growth of III-V semiconductor nanowires on graphene

Ezekiel Anyebe Anyebe[1] | **Manoj Kesaria**[2]

[1] School of Engineering, Cardiff University, Cardiff, UK

[2] School of Physics, Cardiff University, Cardiff, UK

Correspondence
Ezekiel Anyebe Anyebe, School of Engineering, Cardiff University, Cardiff, CF24 3AA, UK.
Email: anyebee@cardiff.ac.uk

Manoj Kesaria, School of Physics, Cardiff University, Cardiff, CF24 3AA, UK.
Email: kesariam@cardiff.ac.uk

Abstract

The recent discovery of the one-atom-thick, two-dimensional graphene layers with exciting properties including superb optical transparency and high mechanical robustness has stimulated extensive research interest for use as an alternative nanowires (NWs) growth platform for applications in next generation, flexible, stretchable, and printable electronic and optoelectronic devices. When combined with the exceptional capabilities of semiconductor NWs including improved light absorption, reduced optical reflectance, enhanced carrier collection, and fast response, the performance of optoelectronic devices could be significantly improved in novel high-performance, flexible nanodevices. However, the growth of semiconductor NWs on 2D graphene layers is highly challenging owing to the absence of surface dangling bonds on graphene. Intriguingly, the last decade has witnessed a flurry of research activity on the growth of III-V semiconductor NWs on graphene. In this review, we highlight the significant advancements that have been made in circumventing this challenge to realize the growth of III-V semiconductor NWs on graphene. We then summarize the recent progress made in the development of graphene-based NWs devices including photodetectors and solar cells. Finally, a brief conclusion and outlook of the way forward in the growth of semiconductor NWs on graphene is presented.

1 | INTRODUCTION

Over the past few decades, semiconducting nanowires (NWs) have emerged as the candidate of choice for the fabrication of next generation high-performance and high sensitivity nanodevices including solar cells,[1] transistors,[2] light emitting diodes,[3] detectors,[4] and other exciting applications such as majorana fermions[5] due to their unique properties including improved light absorption,[6] reduced optical reflectance,[7] enhanced carrier collection,[8] longer diffusion length and lifetime of minority carriers,[9] and fast response[10] relative to conventional planar bulk geometry and epitaxial growth insensitive to lattice matching requirement due to their small footprint which enables elastic strain relaxation.[11,12] Although, NWs are commonly fabricated on Silicon and conventional III-V substrate for several years, the recent discovery of graphene sheets in 2004[13] has stimulated extensive research interest as an alternative platform for NWs growth. This paradigm shifts to the two dimensional (2D) flexible graphene substrate is triggered by the quest to exploit its intriguing

TABLE 1 Comparison of nanowires and bulk thin film growth on graphene

	Nanowires	Bulk thin films
1	Although the wettability of graphene poses a challenge, it is less difficult to nucleate nanowires compared to thin films due to their small footprint	Growth of single crystalline 2D film tends to form rough surfaces with suppression of nucleation due to the relatively poor wettability of graphene[30]
2	Capable of accommodating elastic strain relaxation due to their smaller lateral cross sections[12]	Difficult to accommodating elastic strain relaxation due to large lateral dimensions
3	Their small lateral footprint enables epitaxial growth since they are relatively smaller than the grain size of the stack of graphene layers of graphite at the surface.[33]	The large size of thin films makes them across several graphene grains of graphite suppressing epitaxial growth
4	Nucleation of nanowires in the cubic/hexagonal phase occurs in the (111)/(0001) plane[34] such that the NWs adopt the same hexagonal symmetry as the (0002) - oriented graphitic surface	Nucleation occurs across entire surface making epitaxial growth challenging
5	Requires compliance with strict growth conditions such as restricted domain of temperature window and group V/III flux ratio	Less sensitive to growth conditions with relatively large growth temperature window

properties including excellent electrical[14] and thermal[15] conductivity, high mechanical robustness, and flexibility,[16] superb optical transparency,[17] unique optical properties in printable electronics, flexible, and stretchable devices. Combined with its scalability,[18] relative abundance, and low synthesizing cost,[19] it would provide a unique platform for cost-effective devices. Several graphene based devices have recently been demonstrated including solar cells,[20] and light emitting diodes.[21] More so, the one-atom-thick graphene has demonstrated enormous potential as a low-cost, and flexible transparent conducting electrode.[22] The heteroepitaxial growth of III-V NWs on 2D materials including graphene layer (GP) (note that GP refers to graphene/SiO_2/silicon substrate) and graphitic substrate (GS) (here, few layers of graphite is cleaved and transferred onto silicon substrate) is highly challenging[23] because unlike the growth on conventional III-V semiconductor substrates which are covalently bonded, the non-covalent growth of three dimensional III-V semiconductor materials directly on these non-conventional platforms is not very easy due to the absence of dangling bonds which makes them chemically inert to any foreign atoms[24,25,23]; although this might not be the case with other material systems such as II-VI materials including ZnO which is relatively easier and extensively investigated.[26] More so, the absence of these bonds also heightens the surface tension on the surface and make nucleation difficult.[27] The epitaxial growth of 3D, group III-V materials with sp^3 orbital on 2D layers having sp^2 hybridization is only made possible by weak quasi van der Waals epitaxy (vdWE)[28] which is more tolerant to lattice-matching requirement when compared to conventional epitaxy. Whereas conventional heteroepitaxy is coherent such that a highly lattice mismatched system is characterized by a significant number of strain-induced mismatch-related defects including edge dislocations, threading dislocations, and stacking faults around the heterointerface, VdWE exhibits incommensurate/incoherent in-plane lattices at the heterointerface. As a result, it is possible to epitaxially grow compounds with a large lattice mismatch and different crystalline symmetry to that of the substrate without the usual lattice mismatch induced defects and buffer layers on the vdW substrate.[29] However, the degree of difficulty associated with the growth of III-V semiconductor materials on 2D layers (including GP and GS) is dependent on the nature of the material to be deposited. For instance, there are slight differences in the growth of NWs when compared to bulk thin film as summarized in Table 1. Given the absence of reactive dangling bonds at the epitaxial surface of 2D substrates, their wettability is relatively poor leading to suppression of nucleation[30] which poses a serious challenge for the growth of single-crystalline NWs structures. This limitation is even greater for the growth of 2D thin film which rather favor the formation of rough surfaces[31] and often results in the growth of clusters following the Volmer–Weber growth. In a similar vein, although the vdWE growth of single-crystalline, thin film on the 2D layers significantly relaxes the requirement of lattice matching, the weak interaction between them could result in incommensurate short-range ordering in the epilayer. Even though, such overlayers could nucleate on the layered substrates, it has been demonstrated that there is only a partial epilayer–substrate epitaxial alignment across the epitaxial films resulting in the growth of polycrystalline epilayers with textured grain structure.[30] Alaskar et al[32] demonstrated that the growth of polycrystalline GaAs films on graphene was associated with the weak interactivity of the 2D substrate. On the other hand, although the chemically inert GP/GS

presents a hindrance to NWs growth, the epitaxial growth vertical semiconductor NWs on these surfaces have been successfully demonstrated (as described in Section 2). This could largely be associated with the following[27]: (i) the ability of NWs to accommodate much more lattice mismatch than thin films, due to very efficient elastic relaxation at the lateral free surface,[12] (ii) the small lateral footprint of NWs enables epitaxial growth due to their relatively smaller lateral dimension compared to the grain size of the various A, B, or C stack of graphene layers of graphite (including few layer graphene) at the surface.[33] (iii) the preferential growth of NWs vertically along the [111]/[0001] crystallographic direction for cubic/hexagonal crystal, respectively.[34] Consequently, NWs nucleation in the cubic/hexagonal phase occurs on the (111)/(0001) plane such that the NWs adopt the same hexagonal symmetry as the (0002)-oriented graphitic surface.

Motivated by the need for high performance, flexible, stretchable, and cost-effective optoelectronic nanodevices including flexible displays, printable electronics, sensors, light emitting diodes, and flexible solar cells, there has been an increasing interest in the integration of NWs with the graphene. The last decade has witnessed a flurry of research activity focused on the growth and applications of III-V semiconductor NWs on graphene with significant advances made. Nearly 70% of all these reports were published since the last review by Munshi et al[23] in 2013. This review highlights the recent and significant progress made on the vdWE growth of III-V Semiconductor NWs on GS. More so, despite the recent advances made in the growth of NWs on GS, there are very limited reports of NW/graphene hybrid devices, this review explicates useful strategies for the fabrication of graphene-based NWs device. It is hoped that this review would facilitate an increase in NWs-based graphene device applications.

2 | VAN DER WAALS EPITAXY GROWTH OF SEMICONDUCTOR NANOWIRES ON GRAPHENE

Several growth techniques are being utilized for the growth of III-V Semiconductor NWs on graphene including molecular beam epitaxy (MBE), metal-organic chemical vapor deposition (MOCVD) or metal-organic vapor phase epitaxy (MOVPE) and chemical beam epitaxy (CBE). To facilitate NWs nucleation on the non-covalent, chemically inert graphene substrate (GP), various strategies have been adopted and developed which includes the Au-catalyzed growth which is a dominant technique used for NWs growth. However, Au catalyst poses a serious threat to the electronic and optical properties of NWs as they degrade their material properties[35] and device performance,[36] and are highly detrimental to minority carriers performance due to the introduction of carrier recombination centers such as deep-level traps in the NWs, adversely mitigating its potential for use. As a result, alternative methods have emerged for nucleating III-V semiconductor, such as self-catalyzed growth which involves the use of group III elements to facilitate NWs growth.[37] Selective area vdWE growth technique is also being utilized for site-controlled NWs growth. This involves the deposition of a SiO_x mask layer to cover the GP or GS (henceforth referred to as GP/GS) and selectively etch hole patterns in the mask by electron-beam lithography. In the following section, the various advances made in the growth of binary and ternary III-V NWs will be highlighted.

2.1 | Growth of binary nanowires on graphene

Among all the binary III-V semiconductors, GaAs, GaN, and InAs NWs have been extensively researched materials on GP/GS with nearly half of the available studies focused on InAs material system. The growth and applications of InAs NWs on GP/GS have been extensively studied due to its narrow direct bandgap (0.35 eV), small electron effective mass and high electron mobility of ~30,000 $cm^2\ V^{-1}\ s^{-1}$ at 300 K[38] for applications in high-speed electronics and mid-infrared optoelectronics.[39] They are a perfect candidate for Majorana fermions investigations owing to their large Landé g-factor, strong spin-orbit coupling, and Fermi level pinning in the conduction band.[40,41] On the other hand, GaAs has a direct bandgap and high electron mobility and is the most technologically important compound semiconductor material[42] with highly promising applications in lasers and photodetectors.[43] Similarly, the GaN material is one of the highly interesting and appealing semiconductors for use in high-frequency and high-power devices, light-emitting diodes and lasers owing to its exceptional optical, and electrical properties.[44] Recent progress made in the synthesis of these binary semiconductors is summarized in the following section.

2.1.1 | GaAs nanowires growth

Significant insight into the mechanism of III-V NWs growth on GP/GS by quasi vdWE was given by Munshi et al[27] in 2012 who provided convincing evidence that semiconductor NWs can grow epitaxially on GP/GS. The authors proposed a generic atomic model to describe the possible epitaxial growth configurations by which all conventional III-V semiconductor NWs can be epitaxially

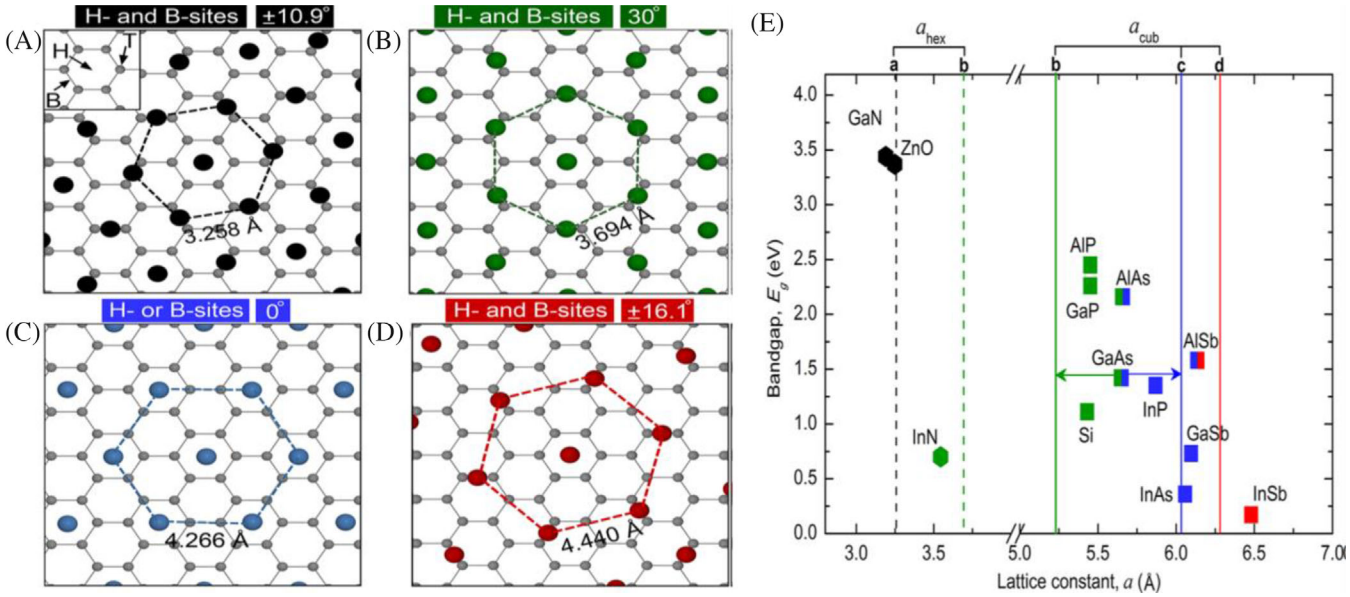

FIGURE 1 Possible semiconductor adsorption sites for epitaxial growth of vertical semiconductor nanowires on graphitic substrates on (1) H- and B-sites (A, B, and D) and (2) H- or B-sites (C). The relative rotations of these hexagons for each atom arrangement are written on the top of each figure. For parts A and D, two relative orientations are possible, ±10.9 and ±16.1°, respectively (only the + rotations are shown in the figures). (E) Lattice constants for the lattice-matched atom arrangements in (A) (black vertical line), (B) (green vertical lines), (C) (blue vertical line), and (D) (red vertical line). Dashed and solid lines correspond to the hexagonal (a_{hex}) and cubic ($a_{cub} = a_{hex} \times \sqrt{2}$) crystal phases of these lattices, respectively. The square (■) and the hexagon (⬢) represent the cubic and hexagonal phases, respectively, for Si, ZnO, and III−V semiconductors. Squares (GaAs, AlAs, AlSb) with two different colors indicate that the semiconductor can adopt either of two atomic arrangements on graphene. Reproduced with permission from.[27] Copyright 2012, American Chemical Society

combined with GP/GS. Owing to the symmetry of a cubic/hexagonal semiconductor in the (111)/(0001) plane, the degree of strain is dependent on the site occupied by the semiconductor on top of the graphene. As shown in Figure 1(A-D), the possible semiconductor adsorption sites on top of graphite are: (1) above the center of the hexagonal carbon rings of graphene (H-site), (2) over the bridge between carbon atoms (B-site) and (3) on the top of a carbon atom (T-site, inset of Figure 1A). A plot of the bandgap energies versus lattice constants of III−V semiconductors is depicted in Figure 1E. Based on this generic model, semiconductors that are nearly lattice-matched to graphene (such as InAs) are expected to adopt the atomic arrangement in Figure 1C whereas those with large lattice mismatch (such as GaAs, AlAs and AlSb) are expected to adopt either of two different atomic arrangements on graphene (Figure 1B or C). The T-site is unfavorable for semiconductor atoms.[27,45] The model was verified experimentally with the growth of vertically aligned GaAs NWs on (GS) via the self-catalyzed vapor-liquid-solid route using MBE. A growth temperature-dependent NWs yield was observed, at a high temperature of 610°C, the NWs density was relatively low (~0.02/μm^2) with the concomitant growth of a high density of spherical Ga particles with high contact angle, which suggest the non-wetting Ga does not favor NWs nucleation.

However, by decreasing the growth temperature to 540°C, the NWs density was significantly increased (~1 μm^{-2}) with a corresponding increase in the density of GaAs parasitic growth. This increased NWs nucleation probability was ascribed to an increase in Ga wetting at a lower temperature, resulting in a smaller contact angle. However, after employing a two-temperature growth regime of NWs nucleated at 540°C for 10 minutes and subsequent growth at 610°C, the NWs density was increased while parasitic growth was suppressed. Transmission Electron Microscopy (TEM) analysis confirmed the epitaxial relationship of as-grown NWs with graphene. GaAs NWs growth on GP/GS is highly challenging and limited to this study possibly due to the high lattice mismatch. Zinc blende (ZB) GaAs (lattice constant = 5.653 Å[46]) NWs if nucleate on the graphene with Ga (or As) atom positioned above both H- and B-sites on graphene[27] (Figure 1B), the distance between two neighboring atoms is 3.694 Å and the lattice mismatch would be 8.2%. On the other hand, if the atoms adopt the atomic arrangement of Figure 1C (above H-sites) on graphene, the distance between two neighboring atoms is 4.266 Å and the corresponding lattice mismatch is 6.3%. This relatively large lattice mismatch explains why it is challenging to realize GaAs NWs growth on GP/GS. This pioneering work provided the laudable impetus for stimulating

interest in the growth of III-V semiconductor NWs on graphite.

2.1.2 | GaN nanowires growth

Adatom mobility on graphene is significantly influenced by the nature and thickness of the graphene[40,47] due to differences in the stability of adatom binding at the graphene edge sites. It is therefore, crucial to investigate the impact of the graphene surface on NWs growth. Several research groups have extensively investigated the growth of GaN NWs on GP/GS using different carrier substrates such as Si, SiO_2, and Al_2O_3. The catalyst-free, epitaxial growth of GaN NWs on graphene by plasma-assisted MBE has been reported.[48] Vertically oriented and dense GaN NWs arrays were selectively deposited on large polycrystalline and small monocrystalline graphene flakes. The graphene flakes were grown by chemical vapor deposition on the SiO_2/Si carrier substrate. The NWs were vertically aligned along their c-axis with an epitaxial relationship with the wurtzite (WZ) GaN, such that the crystallographic $\langle 2\bar{1}\bar{1}0\rangle$ directions of GaN is parallel to carbon zigzag chains. Interestingly, the NWs yield, and length were found to be inversely proportional to the number of graphene layers beneath them; they both decrease rapidly when the layer number increased. A model was developed to explain this trend which was attributed to strain. The optical property of as-grown defect-free GaN NWs was found to be comparable to GaN NWs grown on crystalline Si substrate. This study provided convincing evidence that graphene layers (transferred onto carrier substrates) are a potential replacement for bulk crystalline substrates for the epitaxial growth of GaN NWs based flexible devices.

Graphene is emerging as an alternative substrate for the SAG of GaN NWs. Recently, Morassi et al[49] developed a new approach for the Selective area, growth of vertically aligned GaN NWs on Graphene Nanodots by MBE. NWs growth was achieved on the dots of different sizes 50, 100, 150, and 200 nm. As shown in Figure 2, the average number of NWs per dot significantly increased with growth duration. The NWs were grown on graphene nanodots, patterned by electron beam lithography (EBL) from polycrystalline graphene patches over SiO_2/Si substrates. Vertically aligned GaN NWs ensembles were selectively grown on graphene nanodomains. In addition, the nucleation different sizes dots occurs preferentially on the periphery of the graphene dots, with a linear dependence of the NW number on the dot radius. The study enables epitaxial NWs growth on a single graphene monolayer via lithographic etching which has demonstrated the suitability and enormous potential of this fabrication process. The PL FWHM of GaN NWs on graphene nanodots was comparable to the reference GaN NWs on AlN/Si substrates. A model describing the asymmetric distributions of NW length was presented by considering a dot-size-dependent incubation time. It was shown that NWs incubation time significantly increases for a dot radii below 150 nm, leading to a decreased mean NW length, broader length distribution, and reduced NW filling factor. This graphene SAG technique coupled with the ease with which NW can be removed from the substrate due to the weak van der Waals adhesion to graphene unravels a promising pathway for the fabrication of flexible nanodevices.

Fernández-Garrido[50] investigated the self-assembled formation of GaN NWs by PA-MBE on epitaxial graphene layers with different number of graphene layers synthesized on SiC substrates. Schematic illustration of the different types of graphene layers prepared on 6H-SiC substrates with the corresponding AFM micrographs of the pristine graphene layer as well as the bird's eye SEM view of the GaN NW ensembles, which were prepared on the three different types of graphene layer structures is shown in Figure 3. The study revealed the graphene was etched with the active N species produced by the radio frequency N_2 plasma source at a rate that is, however, several orders of magnitude lower than the GaN deposition rate. As a result, graphene layers in some cases could withstand the growth process as confirmed by Raman spectroscopy and TEM. In addition, the NWs grown on graphene and preferentially nucleated at step edges, are vertically aligned and crystalline with structural quality comparable to those grown on conventional substrates. This study demonstrated a scalable epitaxial technique for the growth of GaN NW on graphene for promising device applications. The self-organized growth of high-density, vertically aligned GaN nanocolumns on multilayer graphene (MLG)/SiO_2 has been reported.[51] A thin AlN buffer layer was used to enhance nucleation as well as to prevent etching of the graphene layer from the impinging active N species produced by the radio frequency N_2 plasma source.[51] TEM analysis revealed the absence of threading dislocations, SFs, or twinning defects. The PL peak intensities of the self-organized GaN nanocolumns is 2.0–2.6 times higher than those on GaN substrate with no yellow luminescence or ZB-phase GaN emission were observed from the nanocolumns. All these studies demonstrate the suitability of the GS for the nucleation and growth of GaN NWs as an alternative to conventional substrates.

2.1.3 | InAs nanowires growth

The pioneering work by Hong et al.[25] in 2011 was the first successful demonstration of InAs NWs on GS by MOVPE via a catalyst-free growth technique. To achieve

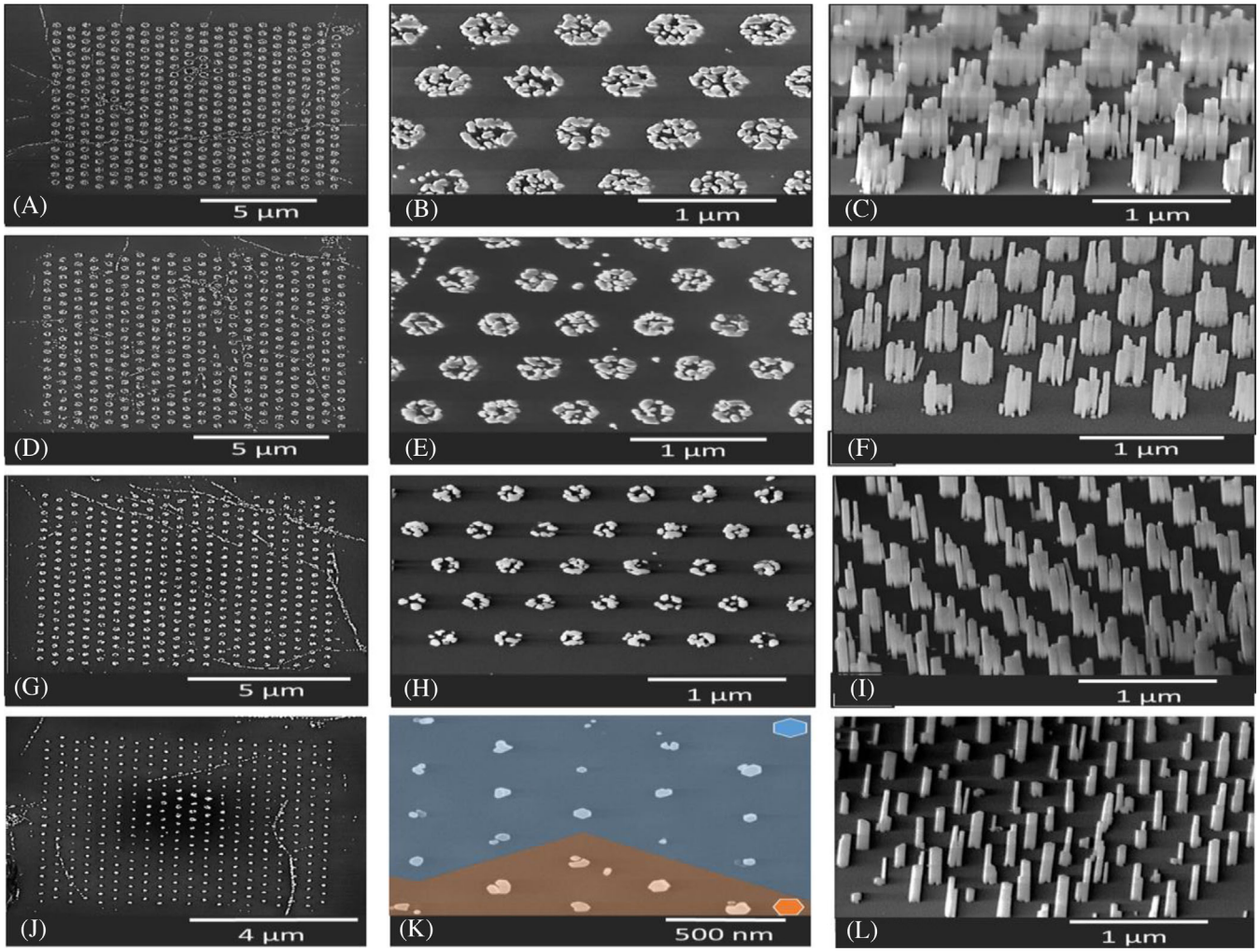

FIGURE 2 (A, B, D, E, G, H, J, K) Top view and (C, F, I, L) 45° tilted SEM images of GaN NWs grown for 4 hours on patterned graphene. The rows correspond to dot radii R_{dot} = 200 nm in (A–C), 150 nm in (D–F), 100 nm in (G–I), and 50 nm in (J–L). Reproduced with permission from.[49] Copyright 2020, American Chemical Society

selective-area vdWE growth, a 20 nm thick SiO_x mask layer was first deposited on the GS by sputtering and oxygen reactive ion etching (O_2 RIE) was used to artificially form monomolecular layer (ML) ledges or kinks on the graphitic surface to facilitate NWs nucleation. Figure 4(A-C) shows the SEM images of as-grown NWs on graphite after 20 minutes of growth. The estimated diameter, length, and density of NWs were measured to be 42±16 nm, 0.8±0.4 μm, and ≈ 6×10^8 cm^{-2}, respectively (Table 2). The non-tapered and vertical directionality of the NWs (Figure 4B) was attributed to the well-optimized growth condition. Figure 4C reveals the hexagonal in-plane alignment (indicated by arrows) of both NWs and Islands owing to the heteroepitaxial relationship between InAs and carbon honeycomb lattice. Conversely, on the non-O_2 RIE etched GS, a dominant Island growth was observed along the naturally formed step-edges of graphitic films (Figure 4D-E). Consequently, the successful heteroepitaxial growth of vertically aligned InAs NWs was attributed to a combination of the controlled atomic layer ledge of the substrate surface and the in-plane lattice matching with the graphitic substrates. As earlier highlighted, InAs are expected to adopt the atomic arrangements of Figure 1C (above H-sites) on graphene. Given the ZB lattice constant of 6.058 Å),[46] and the distance between two neighboring In (or As) atoms is 4.266 Å, the lattice mismatch between InAs and graphite is 0.42%.[27] The controlled growth of vertical NWs with uniform dimension and high yield is highly promising for the fabrication of semiconductor devices on carbon honeycomb lattices. In a separate report by Hung et al,[52] the MOVPE growth of InAs NWs on large-area single-layer graphene (SLG) and multilayer graphene (MLG) films was examined by the vdW heteroepitaxy using the catalyst-free technique to investigate the effect of the surface roughness of graphene on the control of NWs growth direction.

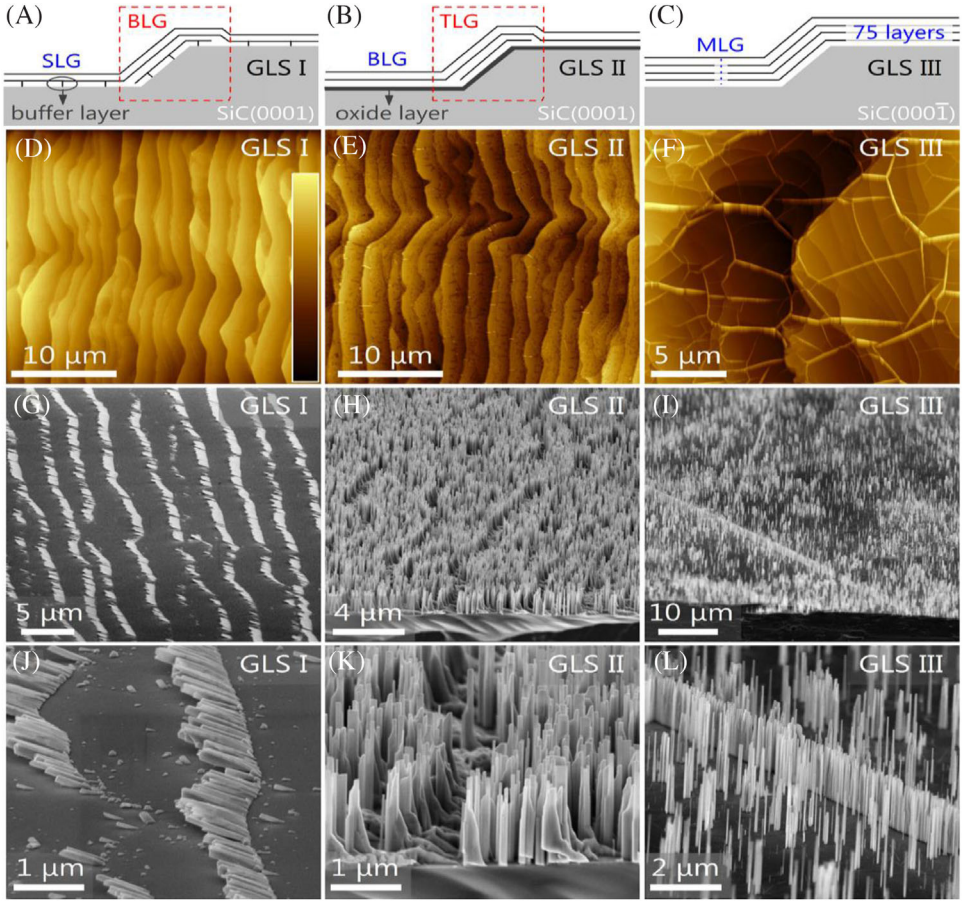

FIGURE 3 Schematic illustration of the (A) Type I, (B) II, and (C) III epitaxial graphene layer structures (GLS) prepared on 6H-SiC substrates. SLG, BLG, TLG, and MLG stand for single-layer, bilayer, trilayer, and multilayer graphene, respectively. (D–F) Atomic force micrographs of the corresponding pristine graphene layer structures. The linear color-code scale bar included in (D) represents 7, 15, and 60 nm in figures (D), (E) and (F), respectively. (G–L) Bird's eye view scanning electron micrographs of the GaN NW ensembles prepared on the three different types of graphene layer structures, as indicated in the images). Reproduced with permission from.[50] Copyright 2017, American Chemical Society

Optical microscopy and Raman spectroscopy were used to confirm the number of stacked layers, thickness and uniformity of the graphene films. Whereas the thickness of the SLG film was highly uniform, the MLG films were nonuniform as depicted in the photographs and surface topographic maps in Figure 5A and B respectively. The thicker MLG films were found to display a higher surface roughness than the SLG due to the presence of many graphene ledges as confirmed by atomic force microscopy. Consequently, the InAs NWs on the SLG films were vertically well aligned with an average density of $(1.6 \pm 0.7) \times 10^8$ cm^{-2} due to the smooth and uniform SLG surface whereas the same growth conditions resulted in vertically less-aligned NWs on the MLG films with an increased number density of $(6.9 \pm 1.1) \times 10^8$ cm^{-2} as shown in the tilted view field-emission SEM images in Figure 5C and D. This demonstrates that high-quality graphene is essential for realizing vertically well-aligned InAs NWs. Furthermore, the authors observed that the CVD-grown GS suppressed the unwanted growth of parasitic InAs.

The self-assisted growth of InAs NWs on graphene by MBE has been reported by Kang.[40] To investigate the influence of the substrate on the morphological and structural properties of the NWs, various graphene substrates were utilized for the growth including bilayer graphene, buffer layer and quasi-free-standing monolayer graphene. The SEM micrograph (Figure 6A,B), of the NWs grown on the bilayer are vertically well-aligned (albeit with the presence of parasitic islands growth) with a diameter of 100 nm and aspect ratio of ~25, however, by switching to a homogenous R30°-reconstructed buffer layer (graphene/SiC interface) substrate, (Figures 6C-D) and adjusting the nucleation conditions, InAs NWs with a significantly smaller diameter of ~35–50 nm, improved aspect-ratio (75–100) and more uniform distribution were realized. The significant improvement in NWs geometry

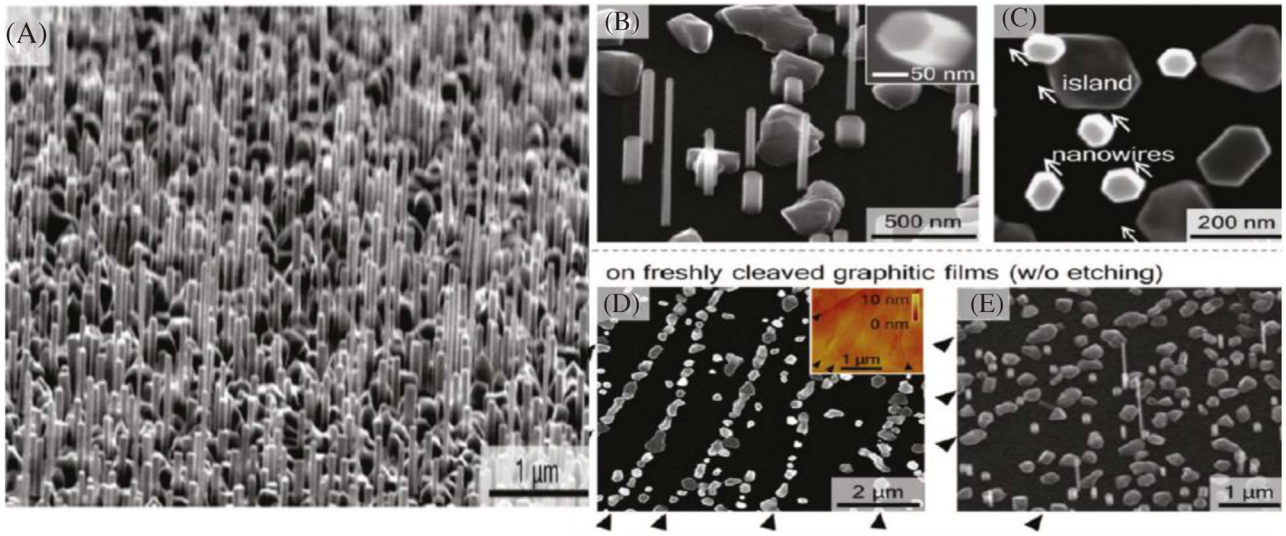

FIGURE 4 InAs nanostructures grown on thin graphitic films. (A-C) SEM images of vertically well-aligned InAs nanowires grown on graphitic films etched by O_2 RIE, taken at (A) 60° tilt view, (B) high magnification 45° tilt view, and (C) top view. (D, E) SEM images of InAs nanostructures grown on non-etched graphitic films, taken at (D) top view and (E) 45° tilt view. Inset in (D) is a surface topographic image of bare graphitic films scanned by AFM. The wedges in peripheries of (D) and (E) indicate the cleaved step-edges of graphitic layers, showing that the InAs nanoislands were mostly yielded specifically along the step-edges of graphitic substrates. Reproduced with permission from.[25] Copyright 2011, American Chemical Society

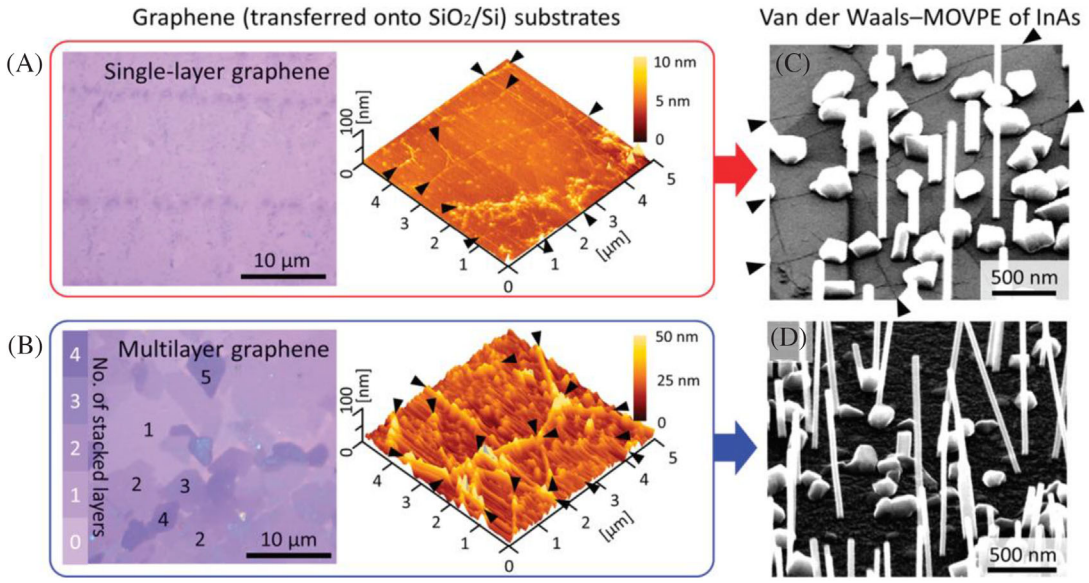

FIGURE 5 InAs nanowires grown on CVD-grown graphene substrates. Optical microscopic image and AFM surface topographic map of (A) SLG and (B) MLG films. Tilt-view FE-SEM images of InAs nanowires grown on (C) SLG and (D) MLG substrates. The wedges indicate graphene wrinkles. Reproduced with permission from.[52] Copyright 2012, American Chemical Society

was attributed to higher corrugation of the buffer layer. This demonstrates that the buffer layer is the better substrate for InAs NWs growth. The authors presented possible evidence that the growth is guided by indium droplets, which are transformed into InAs at the end of the growth evidenced by the rounded NW tips (Figure 6E which is completely different from the flat NWs tip typical of the vapor solid growth mechanism.[39] A 30° orientation configuration of some of the InAs NWs was observed and ascribed to the surface corrugation of the graphene substrate. Low-temperature transport measurements on InAs NW-based devices demonstrated good electric properties; the conductance measurements on the devices displayed a semi-ballistic behavior, while multiple Andreev reflections

TABLE 2 Summary of growth methods and characteristics of III-V nanowires on GS

S/N	Material	Method	Substrate	Growth Strategy	Time [min]	Temp [^{0}C]	L [μm]	D [nm]	Density [x10^8 cm^{-2}]	Remarks	Ref.
1	InAs	MOVPE	Single layer graphene	CF	20	560		40 ±14	(1.6±0.7)	Vertically Aligned	[52]
			Multilayer Graphene films	CF					(6.9±1.1)	Less vertically aligned	
2	InAs	MOVPE	Etched graphite films	SAG	20	560	0.8±0.4	42±16	~ 6		[25]
3	InAs	MBE	Bilayer	SC		450-550		100			[40]
			Buffer layer					~35 -50			
4	InAs	MBE	graphitic flakes	Ag	15	417	10	~20 - 50			[53]
5	InAs	MOCVD	Graphene		10	520 – 580	~3.4	~87	7		[54]
	$InGa_{1-x}As$		Graphene			570				$0.2 < x < 1$	
6	InAs	MBE	Graphite	SC	60	420- 500	2.58±0.34	31.2±6.6	8.09		[55]
	$InAs_{1-x}Sb_x$	MBE	Graphite	SC	120	420- 500	~4.70 ±0.89	~46.0+6.9	1.46	x ~12at. %	

Ag, Silver catalysed growth; CF, catalyst free growth; SAG, Selective area growth; SC, self catalysed growth.

FIGURE 6 A, Bird's-eye view and (B) enlarged SEM micrograph of a single InAs NW grown on bilayer graphene; (C) bird's-eye view and (D) enlarged SEM image of a single InAs NW grown on the buffer layer, showing enhanced 2D growth on the buffer layer; (E) HR-TEM image of the tip of a NW grown on the buffer layer; the * scale bars are 100 nm. Reproduced with permission from.[40] Copyright 2016, IOP publishing Ltd

were observed in the Josephson junction measurements in the non-linear regime, and an inelastic scattering length of about 900 nm was derived. This demonstrates a promising potential for application in InAs NWs-based electronic devices.

To fully exploit the enormous potential of InAs/graphene hybrid junction device applications, it is crucial to optimize epitaxial growth for the precise control of NWs geometry and density.

The size and spatial distribution of NWs can be controllably manipulated using basic growth parameters.[56] Hence, it is essential to investigate the influence of growth parameters of NWs. We[24,57] conducted a comprehensive growth study of InAs NWs on graphite films, mechanically exfoliated from highly oriented pyrolytic graphite (HOPG)

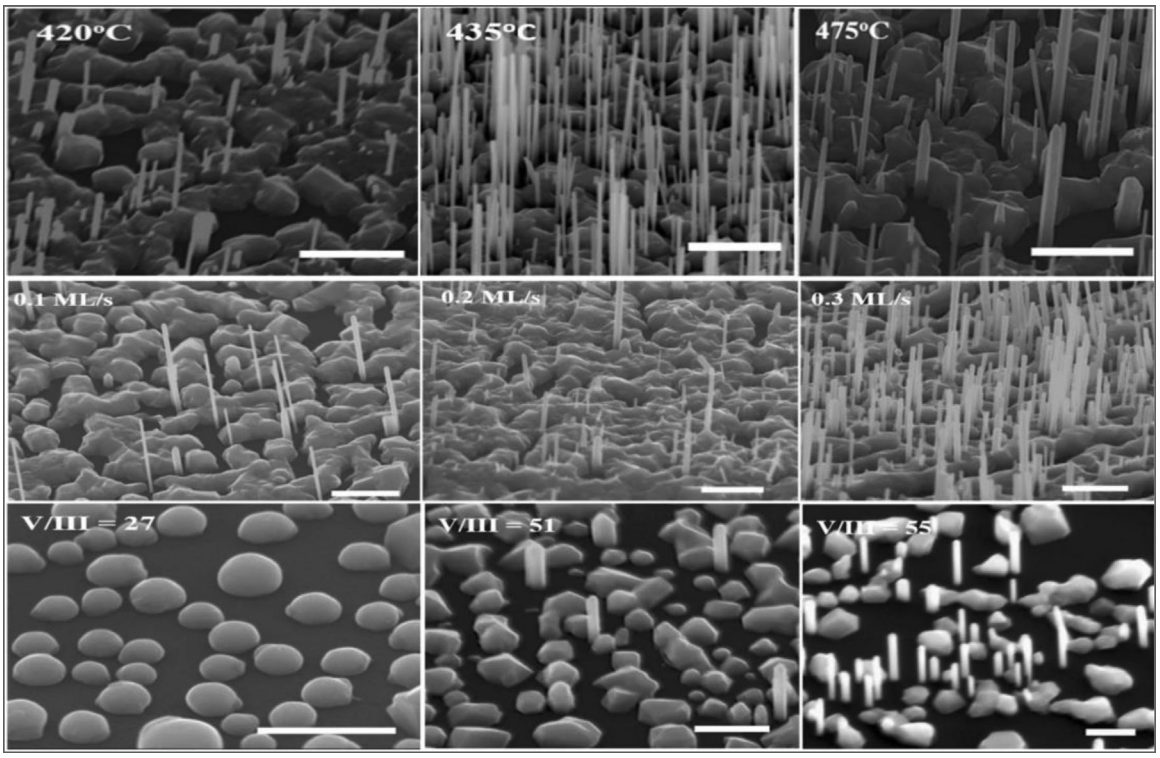

FIGURE 7 45° tilted SEM images of InAs nanowires grown on graphitic substrates as a function of growth temperatures (top panel), growth rates (middle panel) and V/III flux ratios (bottom panel). The scale bars for top and middle panel correspond to 1μm while that of the bottom panel corresponds to 500 nm. (Reproduced from.[24] CC BY 4.0)

using MBE via an Indium droplet-assisted technique. In order to control the morphology and spatial distribution of NWs to realize optimal InAs NWs with high aspect ratio and high density of vertically aligned NWs with superior crystal structure suitable for functional device applications, essential growth parameters including growth temperature, growth rate and V/III flux ratio were varied. The SEM images in Figure 7 (top panel) depicts the variation of InAs NWs density and morphology as a function of growth temperature. As can be seen, the NWs exhibit a homogeneous diameter along their entire length without any measurable tapering. It can be seen that NWs length (L_{NW}) increases for a temperature rise in the range of 400–435°C while it decreases for temperatures beyond 435°C. Maximum L_{NW} was thus obtained at a temperature of 435°C which is in agreement with a previous report.[58] Interestingly, a high density of long and thin NWs with a high aspect ratio (~83) was obtained at an optimal temperature of 435°C (length and diameter of 2.58 ± 0.34 μm and ~31.21 ± 6.59 nm, respectively). However, despite this significantly high aspect ratio, the NWs remain vertically well-aligned without the presence of randomly oriented NWs which demonstrates the feasibility of fabricating InAs NWs with good geometry suitable for fundamental studies such as size-dependent quantum confinement effects. NW growth was realized on GS within the temperature domain of 400–475°C consistent with the MBE growth window of InAs NWs (400–500°C).[39,58,59] For the NWs grown at varying growth rate and fixed temperature and V/III flux ratio, a monotonic increase in NWs density with increasing growth rate was observed (Figure 8, middle panel). With the highest yield of vertically aligned NWs obtained at a relatively high growth rate of 0.3 ML s^{-1}. The observed increase is correlated with the dependence of NWs nucleation on in-flux, with a high in-flux favoring the formation of a high density of In droplets and NWs due to the reduction in adatom diffusion time.[60] Thus, the GS enables NWs growth at high growth rates favorable for cost-effective device fabrication. When the V/III flux ratio was varied while keeping all other precursors fixed (Figure 8, bottom panel), no NWs growth was achieved at a low V/III flux ratio of 27, whereas an increase to 51 enhanced NWs nucleation probability which indicates that As-rich conditions are crucial for the suppression of parasitic growth in favor of InAs NWs growth. This study shows the self-catalyzed growth of InAs NWs with significantly improved morphology can be only achieved within a relatively narrow growth temperature window and restricted domain of growth rate and V/III flux ratio. To elucidate the crystal structures of as-grown InAs NWs, HRTEM measurements were performed. The NWs were found to display a ZB/wurtzite (WZ) crystal phase mixture

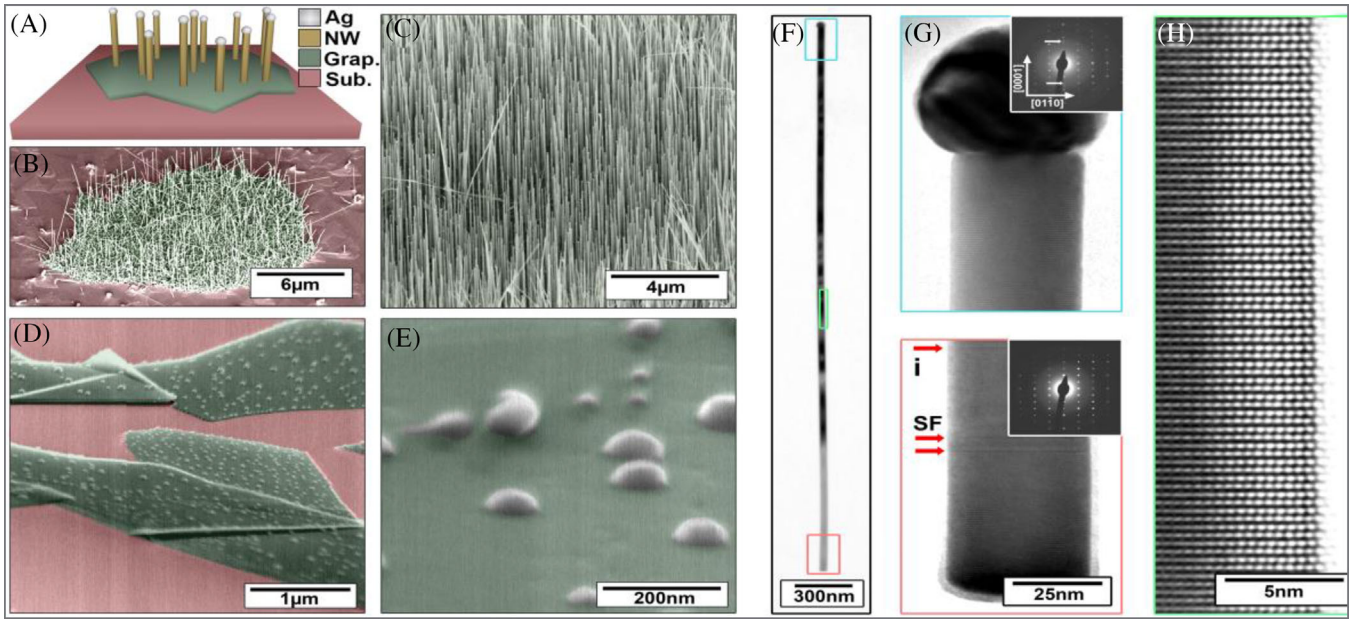

FIGURE 8 Ag-seeded NW growth on graphitic flakes. A, Sketch of the ensemble growth system. (B– E) 45° tilted SEM micrographs of the pre (D-E) and post (B-C) growth system. B, A typical GF with Ag-seeded InAs NWs. Evidently, no NW growth on the bare InAs substrate (false-colored red) is apparent. C, Zoomed in micrograph of vertical Ag-seeded InAs NWs from (b). D, Micrograph of Ag particles on GFs. No Ag particles are visible on the bare InAs substrates. E, Zoomed in micrograph of the post-annealed formation of hemispherical Ag droplets on a GF from (D). (F-H) TEM micrographs of Ag seeded NW grown from a GF as in (B), (C). F, Overview TEM micrograph of the NW (G) Micrograph of a NW top terminated by a Ag seed particle. The inset displays a selected area TEM diffraction pattern with the electron incident beam along the InAs [2-1-10] zone axis with additional peaks along the [0001] direction presumably from the seed particle (white arrows). H, Representative mid-part of a Ag seeded NW demonstrating pure WZ structure. I, Micrograph of the bottom part of the wire presenting three stacking faults highlighted by the red arrows. Reproduced with permission from.[53] Copyright 2016, IOP publishing Ltd

consistent with previous reports of self-assisted InAs NWs[39,61]; however, the defect density (stacking fault and rotational twins) was significantly reduced which is attributed to the well-optimized growth conditions utilized for NWs growth combined with the near coherent in-plane lattice matching between InAs and the graphene honeycomb lattice. Similarly, Baboli et al [62] investigated the pseudo VDE epitaxy growth parameter space for the heterogeneous integration of InAs NWs with continuous films of SLG via MOCVD. By tuning essential growth parameters of growth temperature, V/III ratio, and total flow rate of metalorganic and hydride precursors, the length, diameter, and number density of NWs and areal coverage of parasitic islands, were varied. The study among other things reported that the elimination of a pre-growth in situ AsH_3 surface treatment significantly reduced the coverage of parasitic islands with a concomitant increase in NWs aspect ratio and density. The use of a two-step growth procedure involving a nucleation step at low trimethyl-indium flow rates and a subsequent axial extension step at higher trimethyl-indium flow rate enabled the growth of a high density of high aspect ratio NWs. Optimized growth conditions enabled the growth of high axial growth rate (840 nm min^{-1}), high number density (~8.3×10^8 cm^{-2}) and high aspect ratio (>80) InAs NW arrays on graphitic surfaces. It is believed that this study would provide needed guidance for the vdWE growth of self-assembled III–V semiconductor NWs on two-dimensional monolayer materials for application in flexible optoelectronics and tandem-junction photovoltaics.

Meyer-Holdt[53] explored the Ag-catalyzed InAs NWs growth on transferable graphite flakes (GFs) by MBE. The potential advantage of employing Ag as a catalyst for InAs NWs growth on GFs as a substitute for the commonly used Au was investigated. After depositing Ag on the GFs and the bare InAs substrates ex-situ, the samples were quickly transferred to the MBE growth chamber to minimize Ag oxidation. Figure 8A shows the sketch of the GaAs NWs growth system while SEM images of Figure 8B, C reveals a selective growth of mostly vertically aligned InAs NWs in the [111]/[0001] direction with NWs growth absent on the bare InAs substrate. The 10 μm long and ~20–50 nm thick Ag catalyzed NWs presents a high aspect ratio. The authors believe such selective NWs growth exclusively on the GFs and not on the InAs substrate is less likely using Au as a catalyst due to the extremely long diffusion length of Au on GFs using the growth parameter space utilized for the growth. TEM analysis shows the Ag terminated NW

presents no signs of tapering (f) and the absence of stacking faults (g). The NWs display a pure WZ crystals structure along the entire NW length, except for occasional SFs near the top and bottom, (Figures 8H–I). It was demonstrated that flexible GF/NW ensembles can be transferred to a preferred substrate for characterization and/or device fabrication with enormous potential for a variety of applications. This study unraveled a highly promising pathway for obtaining novel electronic and optical devices based on NW/GF hybrid systems while at the same time enabling fundamental research into the NW/growth substrate interphase as well as parasitic growth. Wallentin et al[63] investigated the Au catalyzed the growth of III−V NWs on graphite by MOVPE. Although vertical NWs were observed for the InP, GaP, and GaAs materials, the highest yield of undoped vertical NWs was obtained for InAs. However, the yield of vertical NWs for GaP and GaAs was strongly improved by supplying the p-dopant DEZn before NWs growth but not by supplying H_2S or HCl. The low NWs yield observed was explained using a classical nucleation model. Graphene has also been shown to partly influence the crystal structure of catalyst-free, vdWE grown InAs nanostructures.[64]

2.2 | Growth of ternary nanowires on graphene

Given the difficulty in realizing III-V NWs growth on graphene, it is not surprising that there are very limited reports of the growth of Ternary NWs on Graphene. The growth of GaAsSb, InAsSb, and InGaAs NWs on GS has been reported in the literature.

2.2.1 | GaAsSb nanowires growth

The growth of high-quality $GaAs_{1-x}Sb_x$ NWs on monolayer graphene by MBE for the application in a flexible near-infrared photodetector has been reported by Nalamati et al.[65] The authors systematically investigated the influence of important growth parameters of growth temperature, V/III beam equivalent pressure (BEP) ratio, and Ga shutter opening duration on NWs growth. A schematic illustration of the growth process of GaAsSb NWs is shown in the top panel of Figure 9. A two step-growth technique of an initial low (520 to 550)°C and subsequent higher (580°C) substrate temperatures along with optimized growth parameters were successfully employed to realize a high yield of vertically oriented GaAsSb NWs on monolayer graphene. On the other hand, a lowered V/III flux ratio enhanced Sb incorporation in as-grown NWs. $GaAs_{1-x}Sb_x$ NWs grown under optimal conditions exhibited a distinct 4 K PL emission peak at 0.94 μm (1.319 eV) with a full width at half maximum (FWHM) of 46 meV. In comparison to the NWs grown on a Si substrate, the GaAsSb NWs on graphene displayed higher intensity and higher optical responsivity majorly due to a lower background carrier concentration coupled with improved carrier mobilities which are signatures of the high optical property of the NWs. Structural analysis of optimal GaAsSb NW (Figure 9 A-D) and SAED patterns (Figure 9E−G) shows a ZB crystal structure of the GaAsSb NWs with microtwins and SFs present exclusively near the NW tip. EDS compositional line scans (Figure 9I−K) indicates a uniform compositional homogeneity along the NW length with an average Sb composition of 7.3 at. %.

2.2.2 | InAsSb nanowires growth

The growth of InAsSb NWs on GS is rare and limited to a study conducted by our group at Lancaster University. High aspect ratio InAs NWs were first obtained on graphite at As-rich conditions to establish optimal growth conditions. SEM analysis reveals the InAs exhibit a uniform NW diameter along the entire length with no visible tapering with an estimated length of 2.58 ± 0.34 μm, the diameter of 31.2 ± 6.6 nm and density of 8.09×10^8 cm^{-2} to give a significantly improved aspect ratio of ~83. This significant improvement is attributed to well-optimized growth conditions. The high yield of vertically well-aligned InAs NWs (InAs[111]‖graphite[0001]) is attributed to the nearly coherent in-plane lattice matching between InAs ⟨110⟩ and graphene ⟨1000⟩.[52,25,54] High-resolution ADF and scanning TEM analysis indicates the InAs/GS NWs are composed of mixed ZB and WZ phases. The growth of high aspect ratio InAsSb NWs which is highly essential for device applications is extremely challenging due to Sb-induced suppression of axial growth and enhancement in radial growth.[66] Anyebe, et al[55] successfully realized for the first time, the growth of high quality, vertically aligned, non-tapered, uniform and ultrahigh aspect ratio InAsSb NWs with Sb composition up to ~12 at. % by indium droplet assisted MBE on graphite. Sb was found to significantly enhance radial growth while suppressing NWs growth at moderately As-rich conditions. We have demonstrated that highly As-rich condition enables the suppression of the Sb surfactant effect to enable the growth of ultrahigh aspect ratio NWs. A combination of X-ray diffraction and PL measurements confirmed the successful Sb incorporation in as-grown NWs evidenced by a distinct redshift in the band-to-band related emission with increasing Sb composition. This study elucidates a promising technique for the monolithic integration of InAsSb NWs on graphitic thin films for high-performance, flexible, and cost-effective optoelectronic devices.

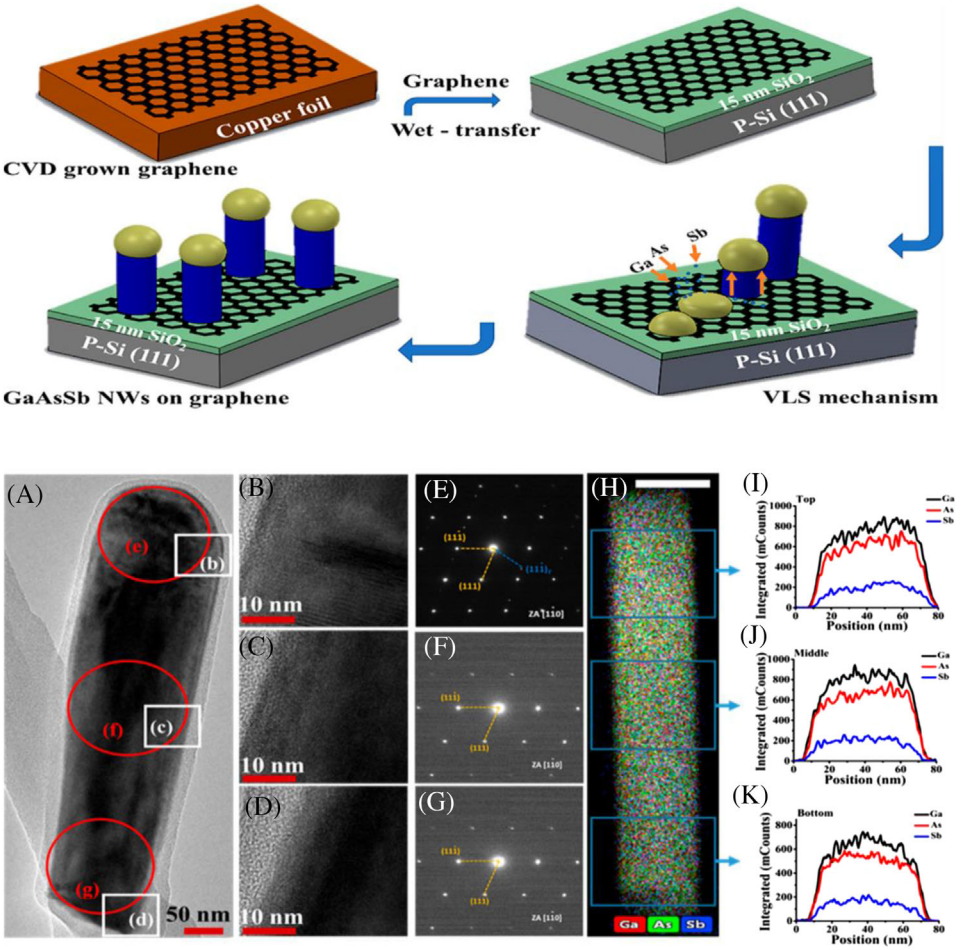

FIGURE 9 Schematic illustration of the growth process of GaAsSb NWs on monolayer graphene (Top panel). TEM image of GaAsSb NW grown on monolayer graphene under optimized conditions. (B-D) HR-TEM images of selected areas marked with white squares in panel (A). (E–G) SAED patterns of selected regions of NW in panel (A), marked with red circles displaying ZB structures viewed from the zone axis of [1$\bar{1}$0]. H, False color mapping of HAADF image of the corresponding NW. (I–K) EDS line scans taken at the top, middle, and bottom segments of the NW marked with blue squares in panel (H). Scale bar is 75 nm for panel (H). Reproduced with permission from.[65] Copyright 2019, American Chemical Society

2.2.3 | InGaAs nanowires growth

The vdWE, MOCVD growth of highly dense arrays of vertically aligned InAs NW and self-organized formation of coaxially heterostructured InAs/$In_xGa_{1-x}As$ NWs, over a wide tunable ternary compositional range, on graphene substrates by Mohseni et al[54] has been reported. First, vertically aligned binary InAs NWs with measured lengths of ~3.4 μm, a diameter of ~87 nm, and a density of 7×10^8 cm^{-2} were deposited. The vertical directionality of as-grown NWs was associated with the near lattice-matching of InAs crystals along the ⟨111⟩ direction on the (0001) graphene surfaces. However, this is growth temperature-dependent as the growth of parasitic islands is promoted at low temperatures below 520°C at the expense of NWs growth which was rather facilitated by higher temperatures ≤ 580°C, beyond which NWs yield is drastically reduced owing to increased desorption of growth precursors. The InAs display a ZB crystal structure with a high density of SFs. The growth of ternary $In_xGa_{1-x}As$ NW was then systematically investigated over a wide composition range ($0.2 < \xi_{In} < 1$) on continuous graphene films where ξ_{In} is the ratio of trimethyl-indium [TMI, $(CH_3)_3In$], to the combined group-III (TMI and trimethyl-gallium [TMG, (CH3)3Ga]) molar flow rates. A compositional inhomogeneity and phase segregation were observed as the growth of InGaAs NWs on graphene spontaneously resulted in phase separation right from the commencement of growth, yielding a distinct InAs–$In_xGa_{1-x}As$ ($0.2 < x < 1$) core–shell segments confirmed by a combination of high-angle annular dark-field (HAADF) imaging and the radial energy dispersive X-ray (EDX) lines can as shown in Figure 10 (A-B), similar to previous reports on Si[67] and GaAs(111)B substrates.[68] The observed

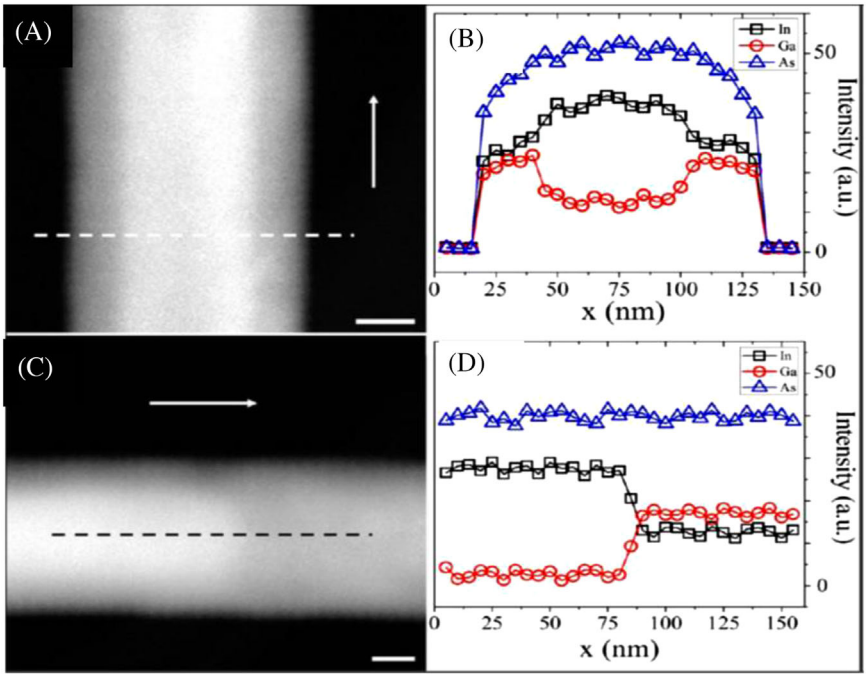

FIGURE 10 Phase-separated InGaAs NW confirmed by (A) HAADF showing a region near the base of a NW ($x = 0.39$). The white dashed line shows the position, x, along which the radial EDX line scan shown in (B) was obtained. C, HAADF image from the central portion of the same NW as in (A). The black dashed line shows the position, x, where the axial EDX line scan shown in (D) was collected. The white arrows in (A) and (C) point toward the NW tip; the scale bars represent a 25 nm length. Black (squares), red (circles), and blue (triangles) data points represent detected counts of elemental In, Ga, and As, respectively. Reproduced with permission from.[54] Copyright 2013, American Chemical Society

self-organized phase separation was found to be unique to the $In_xGa_{1-x}As$ NW growth on graphene, as growth on Si substrates and MoS_2 2D sheets under identical growths conditions yielded the monotonic stoichiometric single phase InGaAs NWs. Which suggests the preferential phase segregation is characteristic of vdWE of a ternary compound, in which a constituent binary compound is nearly lattice-matched to the 2D substrate. In addition, the phenomenon of phase segregation was found not to occur when Au catalyst was utilized to facilitate InGaAs NW growth despite maintaining identical conditions on the same kind of graphene substrates. This phenomenon is highly promising for the fabrication of novel, functional hybrid materials for use in flexible optoelectronic device applications. The catalyst-free, MBE growth and study of the chemical composition and crystal structure of $InAs/In_xGa_{1-x}As$ coaxial nanorod heterostructures on graphene layers has been reported.[69] Cross-sectional electron microscopy investigation indicated that the $In_xGa_{1-x}As$ layers have uniform composition coated hetero-epitaxially to the entire surface of the InAs nanorods, with no interfacial layers or structural defects. A two-step growth method involving a high-temperature growth of InAs nanorods core and a low-temperature coating of $In_xGa_{1-x}As$ shell layers was employed to fabricate $In_xGa_{1-x}As$ shells with precisely controlled chemical composition, thickness, and sharp interface. STEM and EDS analysis confirmed the successful growth of $InAs/In_xGa_{1-x}As$ coaxial nanorod heterostructures which distinctly showed core-shell layers with uniform composition and thickness. A schematic diagram of the TEM sampling positions and the corresponding plan-view is depicted in Figure 11A while a cross-sectional bright-field image of $InAs/In_xGa_{1-x}As$ nanorods, revealing the (0001) surface is shown in Figure 11B. Cross-sectional HR-TEM measurements (Figure 11C) confirmed a clean interface between $In_xGa_{1-x}As$ and InAs. The areas of the oxide layer formed on the nanorod surface and Pt-protection layer are marked in Figure 11D. The HR-TEM images in Figure 11E provided convincing evidence of a clean interface between the InAs nanorod and graphene substrate with no interfacial layer observed. The image also indicates a well-aligned growth direction, parallel to the c axis of the CVD graphene, as shown by the fast Fourier transform (FFT) in the inset. Figure 11F shows the Fourier-filtered images of the interface between InAs and CVD graphene layers. This study explicates a unique route for the monolithic integration of semiconductor coaxial nanorod heterostructures on graphene for novel applications in flexible electronics and optoelectronics.

3 | APPLICATIONS OF VAN DER EPITAXY GROWN NANOWIRES

There are limited reports on GS/InAs devices which is understandable given that the vdWE growth of semiconductor NWs on GS is still in its early years. Here we highlight the recent advances made in the fabrication of optoelectronic devices from NWs deposited on GP/GS.

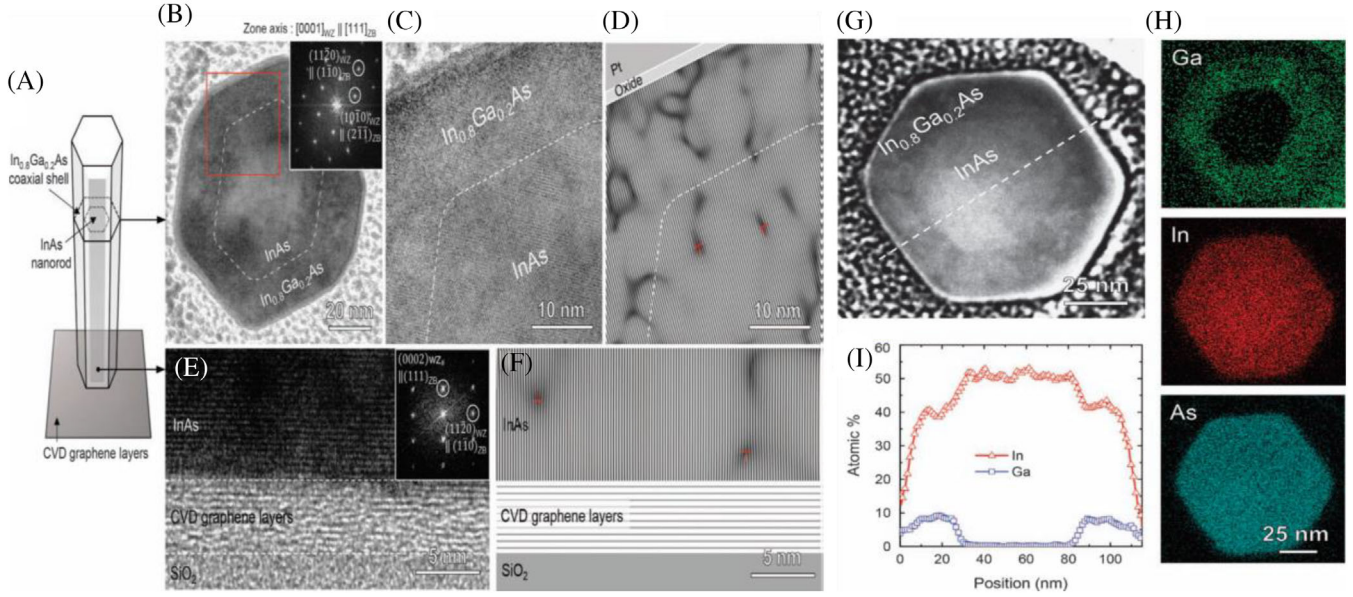

FIGURE 11 Microstructure of InAs/$In_xGa_{1-x}As$ coaxial nanorod heterostructures on CVD graphene layers. A, Schematic diagram of the TEM sampling positions and the corresponding plan-view (B) bright-field-TEM, (C) HR-TEM and (D) Fourier-filtered images of InAs/$In_xGa_{1-x}As$ coaxial nanorod heterostructures. The inset diffraction patterns in b are obtained via FFT of the HR-TEM images in (C). The areas of oxide layer formed on the nanorod surface and Pt-protection layer are marked in (D). Cross-sectional (E) HR-TEM and (F) Fourier-filtered images of the interface between InAs and graphene layers. The inset diffraction patterns in e were obtained via FFT of the corresponding HR-TEM image. Chemical composition of InAs/$In_xGa_{1-x}As$ coaxial nanorod heterostructures grown on CVD graphene layers. G, Plan-view STEM image, (H) elemental mapping of Ga, In and As using STEM–EDS, and (I) EDS line profiles of In and Ga along the dotted line in (G). Reproduced from.[69] CC BY 4.0

3.1 | Device applications of Van der Waals Epitaxy grown nanowires on graphene

In this section the direct applications of nanowires/graphene in hybrid devices are presented including photodetectors and solar cells.

3.1.1 | Photodetector

One of the earliest insight into the responsivity of Graphene/InAs NW heterojunction Photodetectors was provided by Miao et al[70] in 2015. Elsewhere deposited InAs NWs were physically transferred onto graphene substrate and the source/drain electrodes defined on the graphene and NW, respectively, using electron-beam lithography, metallization, and lift-off processes. Figure 12 shows the SEM (a), TEM (b) images and corresponding SAED Pattern (c) of a representative single InAs NW. This new type of graphene/InAs NW vertically stacked heterojunction infrared photodetector (Figure 12 D-G) exhibited a large photoresponsivity of 0.5 AW^{-1} and I_{light}/I_{dark} ratio of 5×10^2, while the photoresponsivity and I_{light}/I_{dark} ratio of graphene infrared photodetectors are 0.1 mAW^{-1}, and 1, respectively. The rectifying behavior of the graphene/InAs NW heterojunctions and the tunable Schottky barrier controls charge transport across the vertically stacked heterostructure was further confirmed by simulations. The study demonstrates that despite the negligible bandgap and small optical absorption of the 2D material, graphene-based infrared detectors are highly promising for the fabrication of graphene-based electronic and optoelectronic devices.

InAs-NWs/graphite heterojunction devices exhibiting rectifying behavior has been demonstrated by Anyebe et al.[24] InAs NWs were directly grown on graphite using an indium droplet assisted growth technique. The devices were processed using standard Photolithography. A layer of SU8 with a thickness of about 4 μm was deposited by spin coating and ultraviolet exposure to encapsulate the NWs. Then, the SU8 was thinned via reactive ion etching using a mixture of O_2 and SF_6 35 sccm and 5 sccm, respectively to free the NW tips. Circular devices with varying diameters (25–200 μm) were defined by a thin gold layer which was deposited on and between the exposed tips of nanowires. To allow electrical connection to the devices, a thicker top contact layer of Ti/Au (20/200 nm) was defined over some specific part of the device area for Ohmic contact. Finally, a back Ohmic contact of aluminum with a thickness of about 200 nm was deposited on the reverse side of the substrate

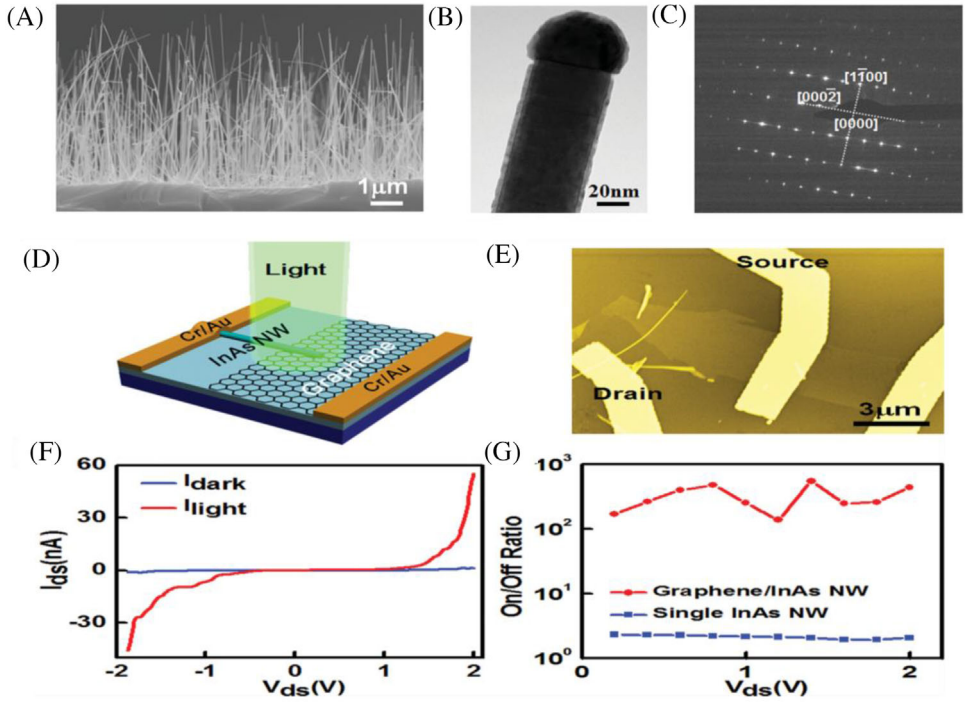

FIGURE 12 A, SEM image of InAs NWs. B, TEM image of a representative single InAs NW and (C) corresponding selected area of electron diffraction (SAED) pattern. A, Schematic of graphene/InAs NW heterojunction near-infrared photodetectors. B, SEM image of graphene/InAs NW heterojunction device. C, Photo-induced *I ds* versus *V ds* output characteristics of graphene/InAs NW heterojunction device. D, Comparison of *I light /I dark* ratios of graphene/InAs NW heterojunction infrared photodetectors and single InAs NW infrared photodetectors. The incident laser wavelength is 1 μm. Reproduced with permission from.[70] Copyright 2015, John Wiley and Sons

to form a complete current loop. Room temperature photovoltaic response with a cutoff wavelength of 3.4 μm was achieved (Figure 13) elucidating a promising route towards the monolithic integration of InAs NWs with graphite for flexible and functional hybrid devices. Self-catalyzed, MBE grown GaAs NW/graphene hybrid heterostructures has also demonstrated huge promise for application in flexible optoelectronic devices. A single GaAs NW photodetector with a high responsivity was demonstrated with no degradation in the optoelectronic material quality, as compared to GaAs NWs grown on GaAs substrates[27] (Figure 14). GaAsSb NWs have also shown high potential for application in flexible near-infrared photodetector. Nalamati et al[65] measured the I–V characteristics of a single vertical GaAsSb NW grown on graphene as well as on Si. The MBE grown GaAsSb NWs on graphene which exhibited significantly lower dark current when compared to those grown on Si.

3.1.2 | Solar cells

A novel solar cell architecture employing a dense array of MOCVD grown, vertically oriented, axial heterostructured InGaAs/InAs NWs with radial p–n junctions and in situ inorganic passivation layers, monolithically grown directly by vdWE on graphene films has been explicated by Mohseni et al.[71] A device performance optimization was conducted by investigating the influence of in situ surface passivation and comparing various device geometries of axial, radial, and passivated radial NW p–n junctions. As schematically depicted in Figure 15 (A–D), after depositing the n-type InAs base segment, the n-type (Si doping) and p-type (Zn doping) In_xGa_{1-x} As ($x \approx 0.25$) sections are sequentially grown. The authors observed that the radial junction geometries show moderate enhancement in power conversion efficiency compared to the axial junction geometries (Figure 15E-F) while the addition of a surface passivation shell was found to be beneficial for mitigating surface defects and Shockley-Read-Hall recombination. Consequently, the device structure in Figure 15C fabricated using a radial p–n junction device structure with an additional in situ grown p-type GaAs shell segment for surface passivation exhibited the optimal device performance. A power conversion efficiencies as high as 2.51% was achieved, which is a new performance record for III-V NWs with embedded junctions grown on graphene and which exceeds previously reported results.[72]

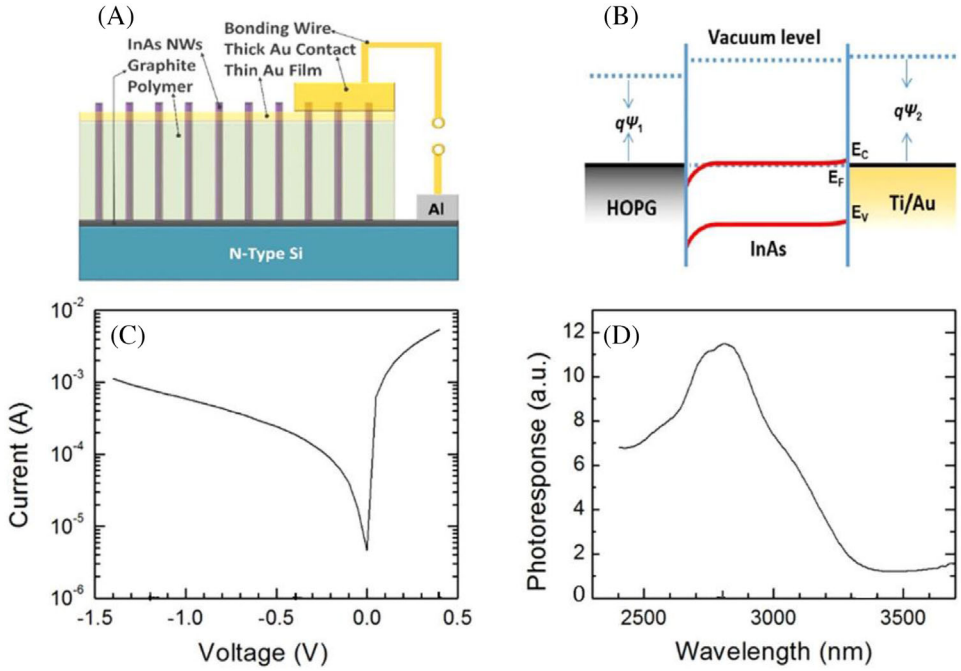

FIGURE 13 Schematic diagram of the NWs ensemble photodetector (**A**), bandgap diagram of InAs/Graphite heterojunction (**B**), I-V curve of a InAs NW ensemble/graphite hybrid device (**C**), and the room temperature spectral photoresponse of the hybrid device (**D**). The device mesa has a diameter of 25 μ m. Reproduced from.[24] CC BY 4.0

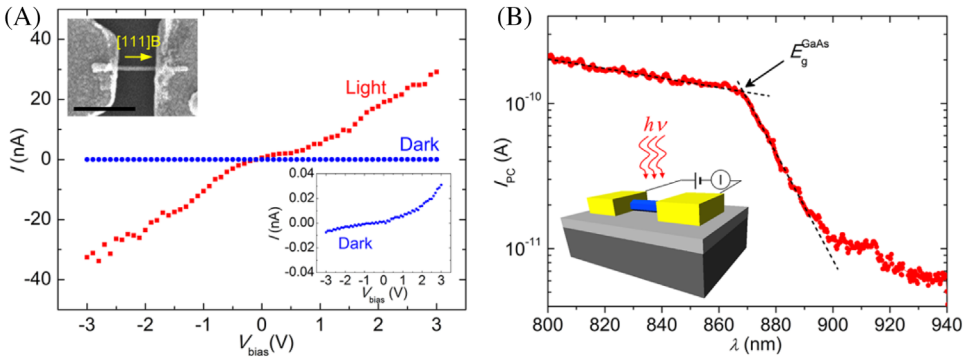

FIGURE 14 Photocurrent response of a single GaAs nanowire photodetector. (A) I−V curves of a single GaAs nanowire photodetector. The blue circles are measured dark current (I_{dark}), whereas the red squares are measured photocurrent (IPC). The photocurrent was measured using an 800 nm laser line with an estimated power density of ~2.5 kW cm^{-2}. The bottom inset shows the dark current with an enlarged y-axis. The top inset is a SEM image of the photodetector where a single nanowire had been dispersed from the same sample, as shown in Figure 2D. The scale bar in the inset is 500 nm. B, Wavelength (λ) dependence of the photocurrent for the nanowire at an applied bias voltage of 50 mV. From the crossing of the black dashed lines, the absorption edge was estimated to be at ~869 nm (1.427 eV) denoted by a black arrow. The inset shows a schematic image of the fabricated nanowire photodetector. Reproduced with permission from.[27] Copyright 2017, American Chemical Society

3.1.3 | Transistors

The exciting potential of graphene-based electronics in terahertz electronics was demonstrated by Liao et al[73] who combined GaN NWs and graphene for the fabrication of high-performance sub-100 nm channel length graphene transistors using a self-aligned approach. The highly doped GaN NW was used as the local gate while the source and drain electrodes were defined through a self-aligned process and the channel length defined by the nanowire size. First, the highly doped n-type GaN NWs were aligned on top of the graphene sheets through a physical dry transfer process as schematically illustrated in Figure 16A, followed by electron beam lithography and metallization (Ti/Au, 50/50 nm) of external source, drain, and top-gate electrodes (Figure 16B). 10 nm Pt metal film was then deposited

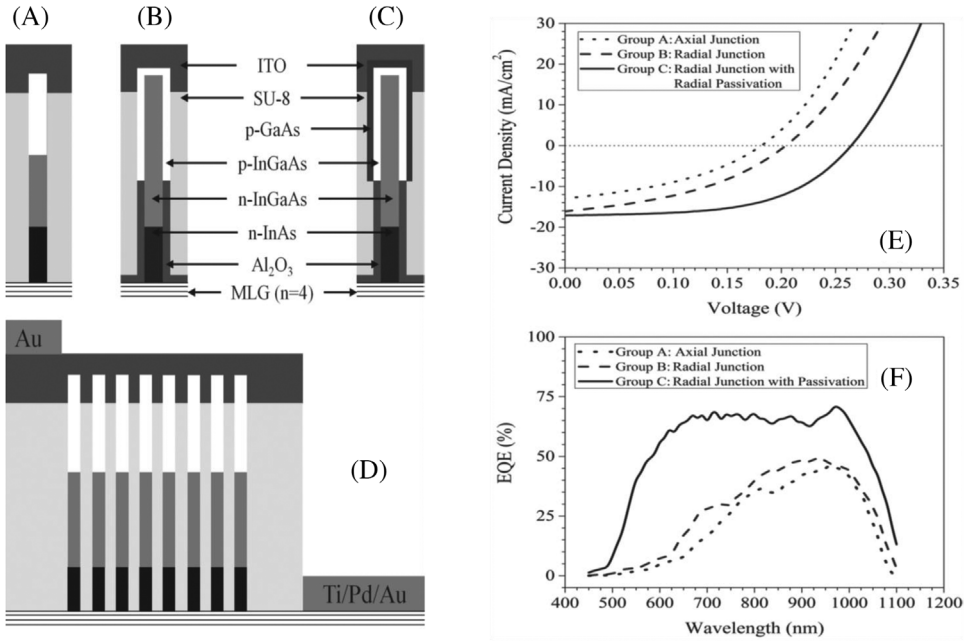

FIGURE 15 Schematic representation of different InGaAs/InAs NW-based device structures of (A) axial p-n junction, (B) radial p–n junctions and (C) passivated radial p–n junctions (D) representation of the metallic contacting scheme. All substrates are depicted as multi-layer graphene (n = 4). E, Illuminated (AM1.5G) I–V characteristics and (F) external quantum efficiency (EQE) spectra measured from the optimal performance of the axial (dotted curve), radial (dashed curve), and passivated radial (solid curve) NW- based solar cells device structure. Reproduced with permission from.[71] Copyright 2014, John Wiley and Sons

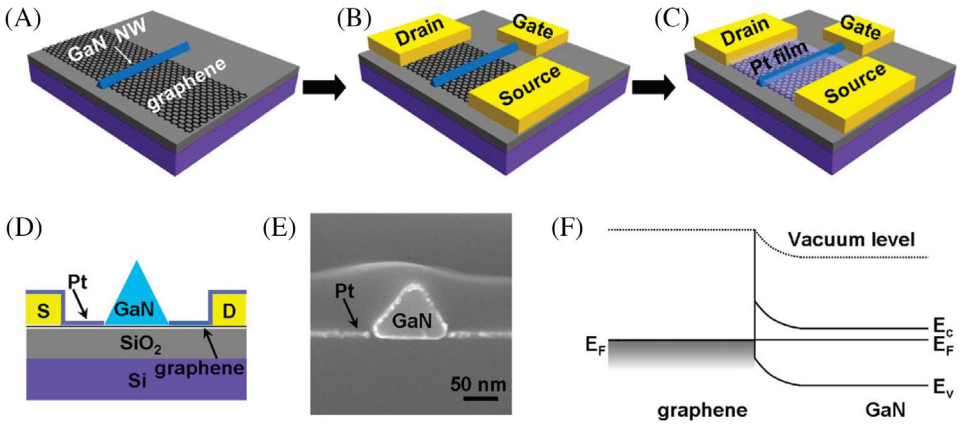

FIGURE 16 Schematic illustration of the fabrication process of the top-gated graphene transistor with a GaN nanowire as the self-aligned top-gate. A, A GaN nanowire is aligned on top of graphene. B, The external source, drain, and top-gate electrodes are fabricated using electron beam lithography. C, Deposition of 10 nm Pt metal film to form the source and drain electrodes self-aligned with the nanowire gate. D, The schematic illustration of the cross section of the device. E, The SEM image of the cross-section of GaN nanowire/graphene device, illustrating well-separated source and drain electrodes due to the nanowire shadow effect. F, Schematic energy band diagrams of a single GaN nanowire on graphene. *E*F, *E*C, and *E*V are Fermi level, conduction band, and valence band, respectively. Reproduced with permission from.[73] Copyright 2010, American Chemical Society

on top of the graphene across the GaN NW to form the source and drain electrodes self-aligned with the NW gate (Figure 16C-E). A Schottky-like barrier (Figure 16F) was created by the contact between the graphene and GaN NW to prevent significant charge leakage between the graphene channel and the GaN NW gate. The interface depletion layer in GaN NW functioned as a "semi-high-*k*" gate dielectric (k ~10), and the GaN NW itself was the local gate. The fabricated graphene transistors with 45–100 nm channel lengths demonstrated a scaled transconductance exceeding 2 mS μm^{-1}, which is comparable to the best performing high electron mobility transistors with

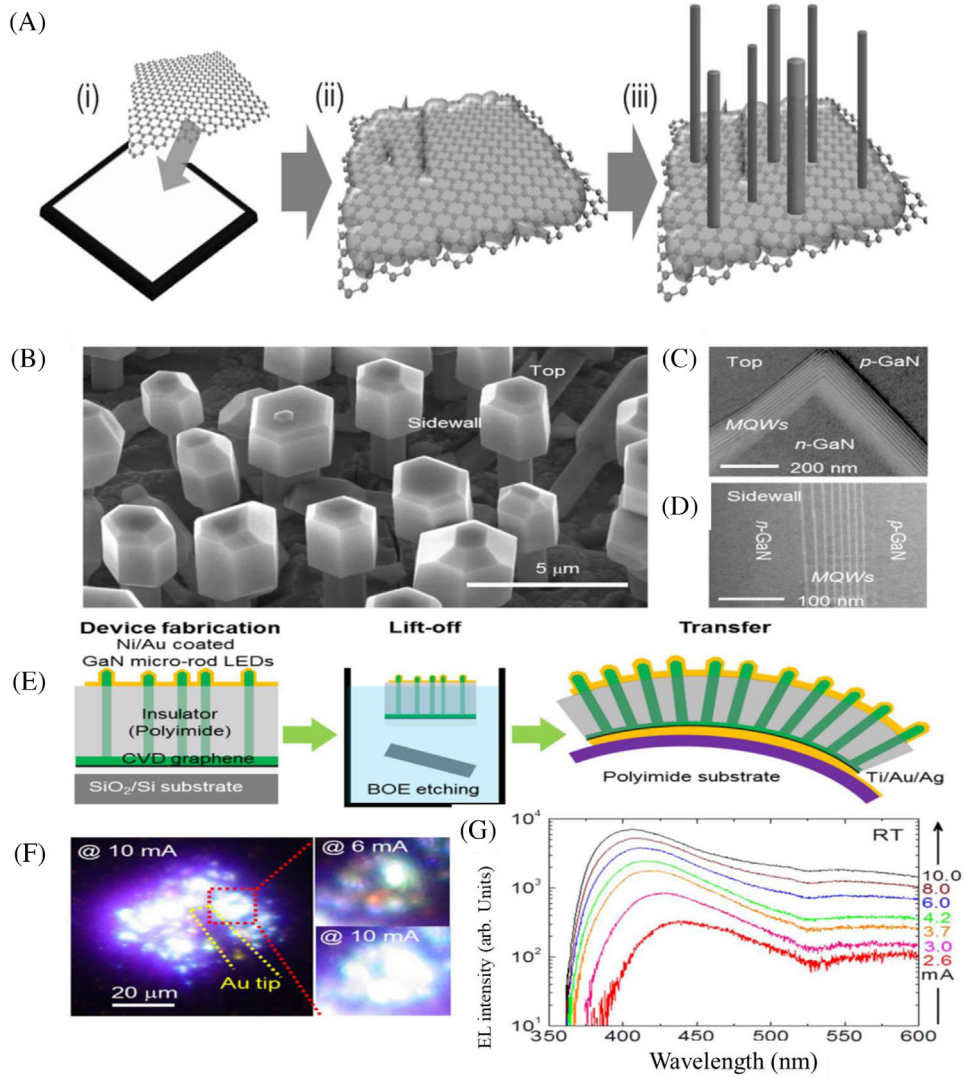

FIGURE 17 Vertical alignment of GaN micro-rods grown on graphene films with and without a GaN buffer layer. A, Schematic illustration of CVD-grown graphene transfer (i), GaN buffer layer growth (ii), and GaN micro-rod growth (iii). GaN micro-rod LEDs fabricated on graphene films. B, An FE-SEM image of coaxial GaN micro-rod LEDs on graphene. Scanning TEM images of (C) the top and (D) the sidewall of the MQW layers on the micro-rod LED. E, A schematic illustration of the fabrication process for vertical structure micro-rod LEDs. F, Magnified optical images of light emission from the LED. G, The power-dependent Electroluminescence spectra at room temperature. Reproduced from.[74] CC BY 4.0

similar channel lengths. A transit time of 120–220 fs and projected intrinsic cutoff frequency (f_T) approaching 700–1400 GHz was demonstrated.

3.2 | Device applications by transfer technology

There is increasing interest in the growth of III-V semiconductor NWs on polymer substrates for the development of flexible, low cost and next-generation optoelectronic devices. However, the epitaxial growth of semiconductor NWs on polymer substrates is highly challenging and the NWs transfer technique to polymer substrates complicated. In addition, the high growth temperatures of III-V semiconductors are incompatible with the low melting temperature of conventional plastic substrates. Interestingly, a highly promising technique for circumventing this problem is the use of transfer technology for the removal of the NWs to polymer substrates after successful growth on two-dimensional substrates (such as graphene) due to the non-covalent, weak VDW bonding between these materials as well as superb mechanical strength.

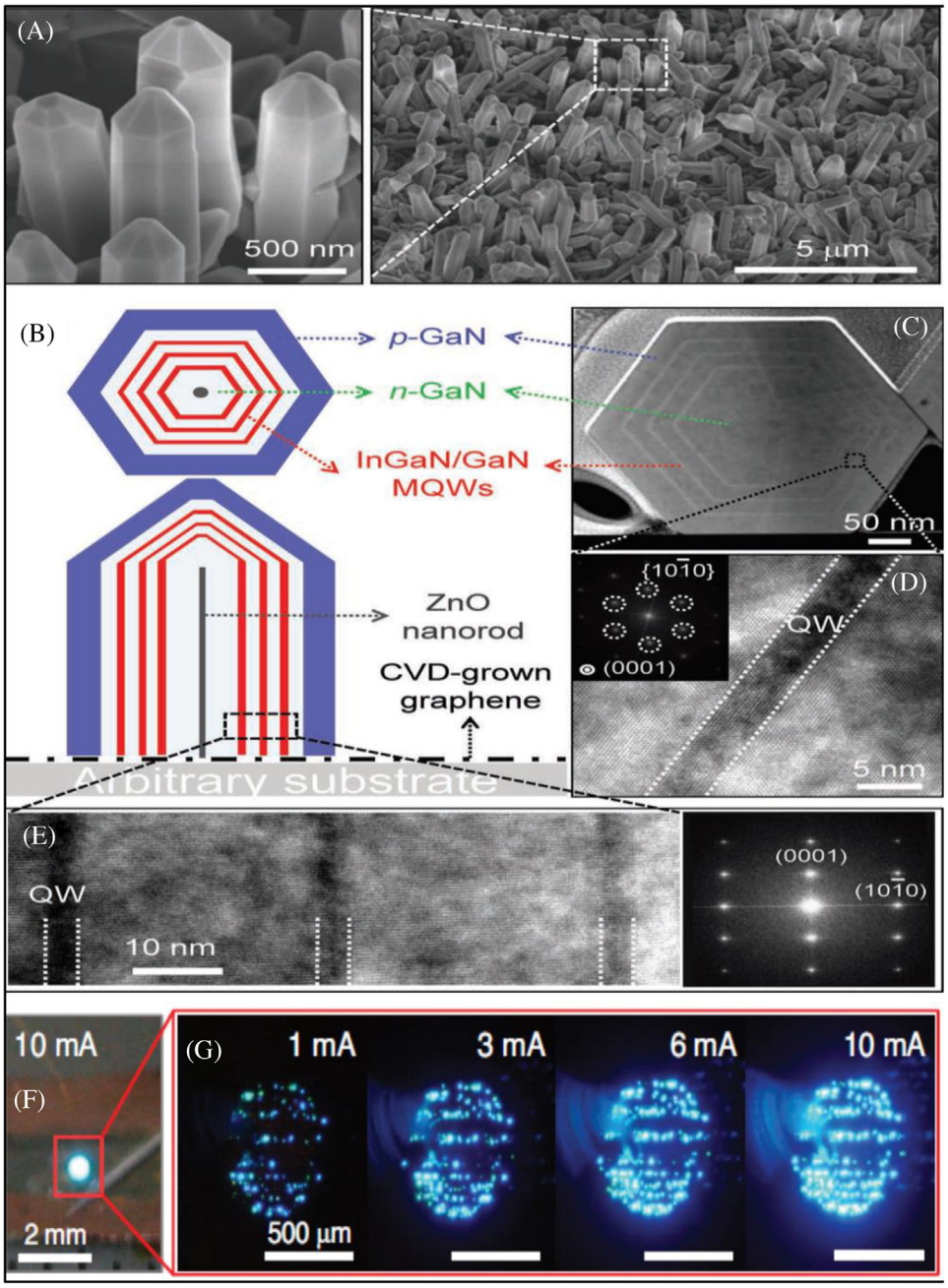

FIGURE 18 GaN-based coaxial LED nanostructures grown directly on graphene films. A, SEM images of GaN-based coaxial LED nanostructures grown on graphene fi lms. Both high- and low-magnification SEM images were obtained at a tilting angle of 30 °. (B,C) Cross-sectional schematic views and STEM image of the coaxially formed GaN-based LED structures. (D,E) High-resolution TEM images of the In x Ga 1– x N/GaN MQW layers and corresponding diffraction patterns obtained via fast Fourier transform. Visible nanostructure LEDs on graphene films. (F) Photograph and (G) optical microscopy images of the light emission from the LED at different applied currents. Reproduced with permission from.[21] Copyright 2011, John Wiley and Sons

3.2.1 | Light-emitting diodes

In 2014, Chung et al[74] reported on the MOCVD growth of GaN micro-rods (MRs) on graphene films which were then transferred to polymer substrates for the fabrication of flexible light emitting diodes (LEDs). Figure 17A schematically illustrates the CVD-grown graphene transfer (i), GaN buffer layer growth (ii), and GaN MRs growth (iii). InGaN/GaN multiple quantum well (MQW) heterostructures and a p-type GaN layer were first deposited coaxially on the GaN MRs before being transferred onto Ag-coated polymer substrates using lift-off technique. As shown in Figure 17B, the GaN micro-rod LEDs are vertically aligned on the graphene substrate following this coating

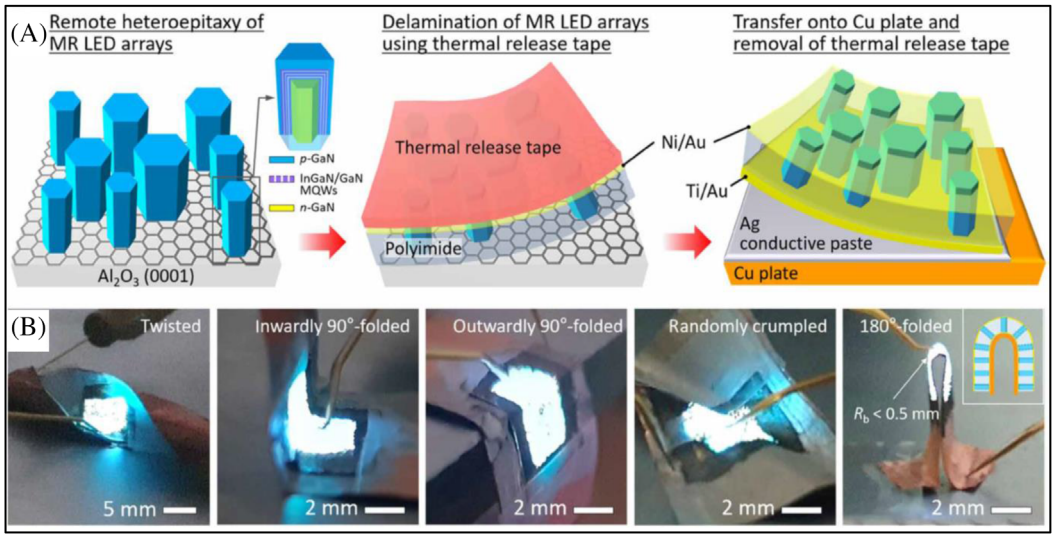

FIGURE 19 Diversely deformable MR LED. A, Schematics illustrating key procedures for fabricating the deformable LED, including remote heteroepitaxy of MR LED arrays and transfer onto conducting metal plate. B, A series of photographs of cyan MR LED ($\lambda = 500$ nm) deformed in various shapes, such as twisted, 90°-folded crumpled, and 180°-folded forms, operated at 100 mA. The inset in the rightmost image of (B) is a schematic illustrating the geometry of MR arrays in the folded form. Reproduced from.[75] CC BY-NC 4.0

process. Scanning TEM images of the top and the sidewall of the MQW layers on the micro-rod LED are depicted in Figure 17C and D respectively. The fabrication of the LEDs was completed by the deposition of metal contacts, and subsequent transfer onto the polymer substrate as shown in Figure 17E. The MRs LEDs exhibited intense emission of visible light, even after transfer onto the flexible polymer substrate, and reliable operation was achieved following numerous cycles of mechanical deformation. Magnified optical images of light emission from the LED and the power-dependent electroluminescence spectra at room temperature are shown in Figure 17 F and G, respectively.

Lee et al[21] reported on the fabrication of flexible inorganic LEDs using GaN/ZnO coaxial nanorod heterostructures grown directly on graphene films by MOVPE. Figure 18 shows the SEM images of the GaN-based coaxial LED nanostructures. First, ZnO nanorods were grown directly on CVD-grown graphene films using catalyst-free MOCVD. Then, a GaN layer was deposited around the circumferences of the ZnO nanorods at a low temperature of 600°C, followed by the growth of a n-GaN layer at a high temperature of 950°C using silane as the doping source. Then, three - period of $In_xGa_{1-x}N$/GaN MQWs were grown at 760 and 850°C, respectively and a Mg-doped p-GaN layer was deposited on top of the GaN quantum barrier layer at 1000°C, using biscyclopentadienyl magnesium as the doping source. As shown in the 10-mA-driven LED photograph (Figure 18E) taken under normal indoor illumination, the blue light emission was very strong and observable with an unaided eye. The optical microscopy image of the light emission from the fabricated GaN-based coaxial LED nanostructures obtained under different applied currents are shown in Figure 18 G. To develop a flexible device, the fabricated LEDs on graphene films were then transferred onto flexible plastic (Cu-coated polyethylene terephthalate) substrate by wet etching of the SiO_2 layer underneath the graphene films with the application of lift off technology. Interestingly, there was no significant degradation of the LED flexible device performance.

Most recently, Jeong et al[75] reported the remote heteroepitaxial MOVPE growth of GaN MRs heterostructures on graphene (single layer graphene) coated c-plane Al_2O_3 (0001) wafer for applications in deformable LEDs. The n-type GaN MRs core was first grown using TMGa and NH_3 precursors with flow rates of 20 and 10–50 standard cubic centimeters per minute, respectively, at 1050°C with hydrogen-diluted silane (SiH_4, 200 parts per million in H_2) as an n-dopant precursor. Then, three-period of InGaN/GaN MQW layers were heteroepitaxially deposited on the n-GaN MRs, and Mg-doped p-GaN was then coated at the outermost shell layer on the MR heterostructures using bis(cyclopentadienyl) magnesium (Cp_2Mg) precursor at 1000°C. To obtain cyan and blue light emissions from the LED arrays, the growth temperature of the InGaN QW was varied from 770° to 800°C, respectively. Ni/Au and Ti/Au ohmic contacts were formed on both the surface of the outmost p-GaN layer and the delaminated bottom surface of n-GaN MRs, respectively for the fabrication of the LED devices. The as-grown MR LED arrays embedded in polyimide film were then transferred onto a conducting Cu plate using thermal release tape as shown in Figure 19A. The MR LED exhibited good electrical and

EL performances with excellent deformability. Intriguingly, the flexible LEDs are capable of withstanding large deformations such as twisted, right-angle inward/outward folds, random crumpling, and 180° folds without any significant degradation to the electroluminescent emission area and color within at least several time extreme deformations (Figure 19B). It is hoped that the versatility of remote epitaxy will enable a gradual transition from current conventional rigid, brittle electronics to flexible, wearable, next-generation electronics.

4 | CONCLUSIONS AND OUTLOOK

Motivated by the need for high performance, flexible, stretchable, and cost-effective optoelectronic nanodevices including flexible displays, printable electronics, sensors, light-emitting diodes, and flexible solar cells, there has been an increasing interest in the growth of NWs on graphene. In this review, we have discussed the challenges and recent progress made in the growth of semiconductor NWs on graphene while highlighting the various growth strategies that have been successfully used to promote the growth of vertically aligned NWs. Then, we summarized the recent advances made in the fabrication of semiconductor NW/graphene hybrid devices. To maximally exploit the enormous benefit of vdWE grown NWs in high-performance GS/NWs hybrid devices, it is essential to establish a better protocol for the reproducible growth of high-density NWs. Consequently, there is a need for further research on the position-controlled selective area growth as well as the controlled self-catalyzed growth of uniform and high-density III-V semiconductors on GP/GS. Furthermore, there is an urgent need for increased research activity on the fabrication of high-performance GS/NWs hybrid devices.

REFERENCES

1. a) P. Krogstrup, H. I. Jorgensen, M. Heiss, O. Demichel, J. V. Holm, M. Aagesen, J. Nygard, A. F. I. Morral, *Nat. Photonics* **2013**, *7*, 306; b) V. Raj, K. Vora, L. Fu, H. H. Tan, C. Jagadish, *ACS Nano* **2019**, *13*, 12015.
2. J. P. Colinge, C. W. Lee, A. Afzalian, N. D. Akhavan, R. Yan, I. Ferain, P. Razavi, B. O'Neill, A. Blake, M. White, A. M. Kelleher, B. McCarthy, R. Murphy, *Nat. Nanotechnol.* **2010**, *5*, 225.
3. H. P. T. Nguyen, S. Zhang, K. Cui, X. Han, S. Fathololoumi, M. Couillard, G. A. Botton, Z. Mi, *Nano Lett*. **2011**, *11*, 1919.
4. a) B. Korzh, Q. Y. Zhao, J. P. Allmaras, S. Frasca, T. M. Autry, E. A. Bersin, A. D. Beyer, R. M. Briggs, B. Bumble, M. Colangelo, G. M. Crouch, A. E. Dane, T. Gerrits, A. E. Lita, F. Marsili, G. Moody, C. Pena, E. Ramirez, J. D. Rezac, N. Sinclair, M. J. Stevens, A. E. Velasco, V. B. Verma, E. E. Wollman, S. Xie, D. Zhu, P. D. Hale, M. Spiropulu, K. L. Silverman, R. P. Mirin, S. W. Nam, A. G. Kozorezov, M. D. Shaw, K. K. Berggren, *Nature Photonics* **2020**, *14*, 250; b) J. Svensson, N. Anttu, N. Vainorius, B. M. Borg, L. E. Wernersson, *Nano Lett*. **2013**, *13*, 1380.
5. V. Mourik, K. Zuo, S. M. Frolov, S. R. Plissard, E. P. A. M. Bakkers, L. P. Kouwenhoven, *Science*. **2012**, *336*, 1003.
6. a) C. H. Kam, H. V. Demir, H. Y. Yu, Q. G. Du, X. W. Sun, *Optics Lett*. **2011**, *35*, 1884; b H. Bao, X. Ruan, *Opt. Lett.* **2010**, *35*, 3378; c) E. Garnett, P. Yang, *Nano Lett*. **2010**, *10*, 1082; d) B. Wang, P. W. Leu, *Opt. Lett.* **2012**, *37*, 3756.
7. a) </number>D. K. Michael, W. B. Shannon, A. P. Jan, B. T.-e. Daniel, C. P. Morgan, L. W. Emily, M. S. Joshua, M. B. Ryan, S. L. Nathan, A. A. Harry, *Nat. Mater* **2010**, *9*, 239; b) J. Zhu, Z. Yu, G. F. Burkhard, C.-M. Hsu, S. T. Connor, Y. Xu, Q. Wang, M. McGehee, S. Fan, Y. Cui, *Nano Lett*. **2009**, *9*, 279; c) C. Lin, M. L. Povinelli, *Opt. Express* **2009**, *17*, 19371; d) L. Hu, G. Chen, *Nano Lett*. **2007**, *7*, 3249.
8. C. Y. Jiang, X. W. Sun, G. Q. Lo, D. L. Kwong, J. X. Wang, *Appl. Phys. Lett.* **2007**, *90*, 263501.
9. G. K. Mor, K. Shankar, M. Paulose, a. Oomman K. Varghese, C. A. Grimes, *Nano Lett*. **2005**, *6*, 215.
10. X. P. Chen, C. K. Y. Wong, C. A. Yuan, G. Q. Zhang, *Sensors Actuators B-Chemical* **2013**, *177*, 178.
11. L. C. Chuang, M. Moewe, C. Chase, N. P. Kobayashi, C. Chang-Hasnain, S. Crankshaw, *Appl. Phys. Lett.* **2007**, *90*, 43115.
12. F. Glas, *Phys. Rev. B Condens. Matter* **2006**, 74.
13. K. S. Novoselov, A. K. Geim, S. V. Morozov, D. Jiang, Y. Zhang, S. V. Dubonos, I. V. Grigorieva, A. A. Firsov, *Science* **2004**, *306*, 666.
14. P. Avouris, *Nano Lett*. **2010**, *10*, 4285.
15. a) A. A. Balandin, S. Ghosh, W. Z. Bao, I. Calizo, D. Teweldebrhan, F. Miao, C. N. Lau, *Nano Lett*. **2008**, *8*, 902; b) J. H. Seol, I. Jo, A. L. Moore, L. Lindsay, Z. H. Aitken, M. T. Pettes, X. S. Li, Z. Yao, R. Huang, D. Broido, N. Mingo, R. S. Ruoff, L. Shi, *Science* **2010**, *328*, 213.
16. a) U. Stoberl, U. Wurstbauer, W. Wegscheider, D. Weiss, J. Eroms, *Appl. Phys. Lett.* **2008**, 93; b) L. Peng, Z. Xu, Z. Liu, Y. Guo, P. Li, C. Gao, *Adv. Mat.* **2017**, 29.
17. R. R. Nair, P. Blake, A. N. Grigorenko, K. S. Novoselov, T. J. Booth, T. Stauber, N. M. R. Peres, A. K. Geim, *Science* **2008**, *320*, 1308.
18. L. G. De-Arco, Y. Zhang, C. W. Schlenker, K. Ryu, M. E. Thompson, C. Zhou, *Nano Lett*. **2010**, *4*, 2865.
19. Y. Okigawa, K. Tsugawa, T. Yamada, M. Ishihara, M. Hasegawa, *Appl. Phys. Lett.* **2013**, 103.
20. a) H. Park, S. Chang, J. Jean, J. J. Cheng, P. T. Araujo, M. Wang, M. G. Bawendi, M. S. Dresselhaus, V. Bulović, J. Kong, S. Gradečak, *Nano Lett*. **2013**, *13*, 233; b) X. Miao, S. Tongay, M. K. Petterson, K. Berke, A. G. Rinzler, B. R. Appleton, A. F. Hebard, *Nano Lett*. **2012**, *12*, 2745.
21. C. h. Lee, Y. j. Kim, Y. J. Hong, S. r. Jeon, S. Bae, B. H. Hong, G. c. Yi, *Adv. Mat.* **2011**, *23*, 4614.
22. a) S. Bae, H. Kim, Y. Lee, X. Xu, J.-S. Park, Y. Zheng, J. Balakrishnan, T. Lei, H. R. Kim, Y. I. Song, Y.-J. Kim, K. S. Kim, B. Ozyilmaz, J.-H. Ahn, B. H. Hong, S. Iijima, *Nature Nanotechnol.* **2010**, *5*, 574; b) J. K. Wassei, R. B. Kaner, *Materials Today* **2010**, *13*, 52.
23. A. M. Munshi, H. Weman, *Physica Status Solidi-RRL* **2013**, *7*, 713. 41
24. E. A. Anyebe, I. Sandall, Z. M. Jin, A. M. Sanchez, M. K. Rajpalke, T. D. Veal, Y. C. Cao, H. D. Li, R. Harvey, Q. D. Zhuang, *Sci. Rep.* **2017**, 7.

25. Y. J. Hong, T. Fukui, *Nano Lett*. **2011**, *5*, 7576.
26. a) Y. J. Kim, J. H. Lee, G. C. Yi, *Appl. Phys. Lett.* **2009**, *95*, 213101; b) B. Kumar, K. Y. Lee, H. Park, S. J. Chae, Y. H. Lee, S. W. Kim, *Acs Nano* **2011**, *5*, 4197; c) Y. J. Kim, Hadiyawarman, A. Yoon, M. Kim, G. C. Yi, C. Liu, *Nanotechnology* **2011**, 22; d) W. I. Park, C. H. Lee, J. M. Lee, N. J. Kim, G. C. Yi, *Nanoscale* **2011**, *3*, 3522.
27. A. M. Munshi, D. L. Dheeraj, V. T. Fauske, D. C. Kim, A. T. J. van Helvoort, B. O. Fimland, H. Weman, *Nano Lett*. **2012**, *12*, 4570.
28. A. Koma, *Thin Solid Films* **1992**, *216*, 72.
29. a) M. I. B. Utama, Q. Zhang, J. Zhang, Y. W. Yuan, F. J. Belarre, J. Arbiol, Q. H. Xiong, *Nanoscale* **2013**, *5*, 3570; b) W. Jaegermann, R. Rudolph, A. Klein, C. Pettenkofer, *Thin Solid Films* **2000**, *380*, 276.
30. S. H. Bae, H. Kum, W. Kong, Y. Kim, C. Choi, B. Lee, P. Lin, Y. Park, J. Kim, *Nat. Mater* **2019**, *18*, 550.
31. a) S. J. Chae, Y. H. Kim, T. H. Seo, D. L. Duong, S. M. Lee, M. H. Park, E. S. Kim, J. J. Bae, S. Y. Lee, H. Jeong, E. K. Suh, C. W. Yang, M. S. Jeong, Y. H. Lee, *RSC Adv.* **2015**, *5*, 1343; b) P. Gupta, A. A. Rahman, N. Hatui, M. R. Gokhale, M. M. Deshmukh, A. Bhattacharya, *J. Cryst. Growth* **2013**, *372*, 105.
32. Y. Alaskar, S. Arafin, Q. Y. Lin, D. Wickramaratne, J. McKay, A. G. Norman, Z. Zhang, L. C. Yao, F. Ding, J. Zou, M. S. Goorsky, R. K. Lake, M. A. Zurbuchen, K. L. Wang, *J. Cryst. Growth* **2015**, *425*, 268.
33. J. Hass, W. A. de Heer, E. H. Conrad, *J Phys-Condens Matter* **2008**, 20.
34. a) J. Johansson, L. S. Karlsson, C. P. T. Svensson, T. Martensson, B. A. Wacaser, K. Deppert, L. Samuelson, W. Seifert, *Nat. Mater* **2006**, *5*, 574; b) V. Schmidt, J. V. Wittemann, S. Senz, U. Gosele, *Adv. Mat.* **2009**, *21*, 2681.
35. a) M. Silhavik, M. Muller, J. Stuchlik, H. Stuchlikova, M. Klementova, J. Kocka, A. Fejfar, J. Cervenka, *Appl. Phys. Lett.* **2019**, 114; b) P. Liang, Y. Liu, H. B. Shu, Q. M. Dong, L. Wang, T. Shen, *Solid State Commun*. **2014**, *183*, 8; c) J. E. Allen, E. R. Hemesath, D. E. Perea, J. L. Lensch-Falk, Z. Y. Li, F. Yin, M. H. Gass, P. Wang, A. L. Bleloch, R. E. Palmer, L. J. Lauhon, *Nat. Nanotechnol.* **2008**, *3*, 168; d) A. J. T. a. S. J. Pearton, *J Phys C: Solid State Phys* **1983**, *16*, 1665; e) W. H. Chen, L. W. Yu, S. Misra, Z. Fan, P. Pareige, G. Patriarche, S. Bouchoule, P. R. I. Cabarrocas, *Nat. Commun.* **2014**, 5; f) E. A. Anyebe, *Nanomaterials* **2020**, *10*, 2064.
36. V. T. Renard, M. Jublot, P. Gergaud, P. Cherns, D. Rouchon, A. Chabli, V. Jousseaume, *Nat. Nanotechnol.* **2009**, *4*, 654.
37. K. A. Dick, P. Caroff, *Nanoscale* **2014**, *6*, 3006.
38. a) X. Wallart, J. Lastennet, D. Vignaud, F. Mollot, *Appl. Phys. Lett.* **2005**, *87*, 43504; b) S.-G. Ihn, J.-I. Song, *Nanotechnology* **2007**, *18*, 355603.
39. E. Dimakis, J. Lähnemann, U. Jahn, S. Breuer, M. Hilse, L. Geelhaar, H. Riechert, *Cryst. Growth Des.* **2011**, *11*, 4001.
40. J.-h. Kang, Y. Ronen, Y. Cohen, D. Convertino, A. Rossi, C. Coletti, S. Heun, L. Sorba, P. Kacman, H. Shtrikman, *Semicond Sci Technol* **2016**, *31*, 115005.
41. A. Das, Y. Ronen, Y. Most, Y. Oreg, M. Heiblum, H. Shtrikman, *Nat. Physics* **2012**, *8*, 887.
42. S. Adachi, *GaAs and related materials: bulk semiconducting and superlattice properties*, World Scientific, Singapore **1994**.
43. B. Hua, J. Motohisa, Y. Ding, S. Hara, T. Fukui, *Appl. Phys. Lett.* **2007**, 91.
44. a) J. B. Schlager, N. A. Sanford, K. A. Bertness, A. Roshko, *J. Appl. Phys.* **2011**, 109; b) Q. M. Li, J. B. Wright, W. W. Chow, T. S. Luk, I. Brener, L. F. Lester, G. T. Wang, *Opt. Express* **2012**, *20*, 17873; c) K. A. Bertness, Ieee, 2014 Ieee Photonics Society Summer Topical Meeting Series **2014**, 32.
45. K. Nakada, A. Ishii, *Solid State Commun*. **2011**, *151*, 13.
46. I. Vurgaftman, J. R. Meyer, L. R. Ram-Mohan, *J. Appl. Phys.* **2001**, *89*, 5815.
47. a) T. P. Hardcastle, C. R. Seabourne, R. Zan, R. M. D. Brydson, U. Bangert, Q. M. Ramasse, K. S. Novoselov, A. J. Scott, *Phys. Rev. B Condens. Matter* **2013**, 87; b) S. W. Poon, W. Chen, E. S. Tok, A. T. S. Wee, *Appl. Phys. Lett.* **2008**, 92.
48. V. Kumaresan, L. Largeau, A. Madouri, F. Glas, H. Z. Zhang, F. Oehler, A. Cavanna, A. Babichev, L. Travers, N. Gogneau, M. Tchernycheva, J. C. Harmand, *Nano Lett*. **2016**, *16*, 4895. 42
49. M. Morassi, N. Guan, V. G. Dubrovskii, Y. Berdnikov, C. Barbier, L. Mancini, L. Largeau, A. V. Kumaresan, F. H. Julien, L. Travers, N. Gogneau, J. C. Harmand, M. Tchernycheva, *Cryst. Growth Des.* **2020**, *20*, 552.
50. S. Fernandez-Garrido, M. Ramsteiner, G. H. Gao, L. A. Galves, B. Sharma, P. Corfdir, G. Calabrese, Z. D. Schiaber, C. Pfuller, A. Trampert, J. M. J. Lopes, O. Brandt, L. Geelhaar, *Nano Lett*. **2017**, *17*, 5213.
51. H. Hayashi, Y. Konno, K. Kishino, *Nanotechnology* **2016**, 27.
52. Y. J. Hong, W. H. Lee, Y. Wu, R. S. Ruoff, T. Fukui, *Nano Lett*. **2012**, *12*, 1431.
53. J. Meyer-Holdt, T. Kanne, J. E. Sestoft, A. Gejl, L. Zeng, E. Johnson, E. Olsson, J. Nygård, P. Krogstrup, *Nanotechnology* **2016**, *27*, 365603.
54. P. K. Mohseni, A. Behnam, J. D. Wood, C. D. English, J. W. Lyding, E. Pop, X. L. Li, *Nano Lett*. **2013**, *13*, 1153.
55. E. A. Anyebe, Q. Zhuang, B. J. Robinson, O. Kolosov, M. K. Rajpalke, T. D. Veal, V. Falko, *Nano. Lett.* **2015**, *15*, 4348.
56. a) H. J. Joyce, J. Wong-Leung, Q. Gao, H. H. Tan, C. Jagadish, *Nano Lett*. **2010**, *10*, 908; b) K. A. Dick, P. Caroff, J. Bolinsson, M. E. Messing, J. Johansson, K. Deppert, L. R. Wallenberg, L. Samuelson, *Semicond Sci Technol* **2010**, *25*, 24009.
57. Q. D. Zhuang, E. A. Anyebe, A. M. Sanchez, M. K. Rajpalke, T. D. Veal, A. Zhukov, B. J. Robinson, F. Anderson, O. Kolosov, V. Fal'ko, *Nanoscale Res. Lett.* **2014**, *9*, 321.
58. G. Koblmüller, S. Hertenberger, K. Vizbaras, M. Bichler, F. Bao, J. P. Zhang, G. Abstreiter, *Nanotechnology* **2010**, *21*, 365602.
59. S. Hertenberger, D. Rudolph, J. Becker, Bichler, J. J. Finley, G. Abstreiter, G. Koblmüller, *Nanotechnology* **2012**, *23*, 235602.
60. E. A. Anyebe, Q. Zhuang, A. M. Sanchez, S. Lawson, A. J. Robson, L. Ponomarenko, A. Zhukov, O. Kolosov, *Physica Status Solidi - Rapid Research Letters* **2014**, 8.
61. a) W. Wei, X. Y. Bao, C. Soci, Y. Ding, Z. L. Wang, D. Wang, *Nano Lett*. **2009**, *9*, 2926; b) Y. Jing, X. Bao, W. Wei, C. Li, K. Sun, D. P. R. Aplin, Y. Ding, Z.-L. Wang, Y. Bando, D. Wang, *J. Phys. Chem. C* **2014**, *118*, 1696.
62. M. A. Baboli, M. A. Slocum, H. Kum, T. S. Wilhelm, S. J. Polly, S. M. Hubbard, P. K. Mohseni, *Crysteng Commun.* **2019**, *21*, 602.
63. J. Wallentin, D. Kriegner, J. Stangl, M. T. Borgström, *Nano Lett*. **2014**, *14*, 1707.
64. J. E. Choi, J. Yoo, D. Lee, Y. J. Hong, T. Fukui, *Appl. Phys. Lett.* **2018**, 112.
65. S. Nalamati, M. Sharma, P. Deshmukh, J. Kronz, R. Lavelle, D. Snyder, C. L. Reynolds, Y. Liu, S. Iyer, *ACS Appl. Nano Mater.* **2019**, *2*, 4528.

66. E. A. Anyebe, M. K. Rajpalke, T. D. Veal, C. J. Jin, Z. M. Wang, Q. D. Zhuang, *Nano Res.* **2015**, *8*, 1309.
67. S. Hertenberger, S. Funk, K. Vizbaras, A. Yadav, D. Rudolph, J. Becker, S. Bolte, M. Doblinger, M. Bichler, G. Scarpa, P. Lugli, I. Zardo, J. J. Finley, M. C. Amann, G. Abstreiter, G. Koblmuller, *Appl. Phys. Lett.* **2012**, 101.
68. Y. N. Guo, H. Y. Xu, G. J. Auchterlonie, T. Burgess, H. J. Joyce, Q. Gao, H. H. Tan, C. Jagadish, H. B. Shu, X. S. Chen, W. Lu, Y. Kim, J. Zou, *Nano Lett.* **2013**, *13*, 643.
69. Y. Tchoe, J. Jo, M. Kim, G.-C. Yi, *NPG Asia Mater.* **2015**, *7*, e206. 40
70. J. S. Miao, W. D. Hu, N. Guo, Z. Y. Lu, X. Q. Liu, L. Liao, P. P. Chen, T. Jiang, S. W. Wu, J. C. Ho, L. Wang, X. S. Chen, W. Lu, *Small* **2015**, *11*, 936.
71. P. K. Mohseni, A. Behnam, J. D. Wood, X. Zhao, K. J. Yu, N. C. Wang, A. Rockett, J. A. Rogers, J. W. Lyding, E. Pop, X. Li, *Adv. Mater.* **2014**, *26*, 3755.
72. R. R. LaPierre, A. C. E. Chia, S. J. Gibson, C. M. Haapamaki, J. Boulanger, R. Yee, P. Kuyanov, J. Zhang, N. Tajik, N. Jewell, K. M. A. Rahman, *Physica Status Solidi-RRL* **2013**, *7*, 815.
73. L. Liao, Y. C. Lin, M. Q. Bao, R. Cheng, J. W. Bai, Y. A. Liu, Y. Q. Qu, K. L. Wang, Y. Huang, X. F. Duan, *Nature* **2010**, *467*, 305.
74. K. Chung, H. Beak, Y. Tchoe, H. Oh, H. Yoo, M. Kim, G.-C. Yi, *APL Mater.* **2014**, *2*, 092512.
75. J. Jeong, Q. X. Wang, J. Cha, D. K. Jin, D. H. Shin, S. Kwon, B. K. Kang, J. H. Jang, W. S. Yang, Y. S. Choi, J. Yoo, J. K. Kim, C. H. Lee, S. Lee, A. A. Zakhidov, S. Hong, M. J. Kim, Y. J. Hong, *Sci. Adv.* **2020**, 6.

How to cite this article: Anyebe EA, Kesaria M. Recent advances in the Van der Waals epitaxy growth of III-V semiconductor nanowires on graphene. *Nano Select*. 2020;1-24.
https://doi.org/10.1002/nano.202000142